> Banner appropriate to article type will appear here in typeset article

Role of non-linearities induced by deterministic forcing in the low-frequency dynamics of transitional shock wave/boundary layer interaction

Mariadebora Mauriello[1]†, Pushpender K Sharma[1], Lionel Larchevêque[2] and Neil D Sandham[1]

[1]Department of Aeronautics and Astronautics, University of Southampton, Boldrewood Innovation Campus, Southampton S016 7QF United Kingdom,

[2]Aix-Marseille Univ, CNRS, IUSTI, Marseille, France.

Direct numerical simulations are carried out to investigate the underlying mechanism of the low-frequency unsteadiness of a transitional shock reflection with separation at $M = 1.5$. To clarify the nonlinear mechanisms, the incoming laminar boundary layer is forced with two different arrangements of oblique unstable modes. Each wave arrangement is given by a combination of two unstable waves such that their difference in frequency falls in a low frequency range corresponding to a Strouhal number (based on the length of interaction) of 0.04. This deterministic forcing allows the introduction of nonlinearities, and high-order statistical tools are used to identify the properties of quadratic couplings. It is found that the low-frequency unsteadiness and the transition to turbulence are decoupled problems. On the one hand, the unstable modes of the boundary layer interact non-linearly such that energy cascades to higher frequencies, initiating the turbulent cascade process, and to lower frequencies. On the other hand, the low-frequency quadratic coupling of the oblique modes is found to be responsible for low-frequency unsteadiness affecting the separation point. The direction of the quadratic interactions is extracted and it is shown that, in the presence of low-frequency unsteadiness, these interactions enter the separated zone just before reattachment and travel both downstream and upstream, extending beyond the separation point, hence feeding the low-frequency bubble response. In addition to the two main arrangements of oblique modes, two other combinations are analysed, including multiple oblique waves and streaks. Interestingly, their inclusion did not alter the low-frequency unsteadiness phenomenon. Furthermore, the effect of the forcing difference frequency is examined and it is shown that the breathing phenomenon is sensitive to the range of frequencies present in the system due to a low-pass filter effect.

Key words:

† Email address for correspondence: mariadebora.mauriello@soton.ac.uk

Abstract must not spill onto p.2

1. Introduction

In high speed flows, the interaction between shock waves and the boundary layer is a common phenomenon. This interaction, referred to in the literature as SBLI, can have significant effects on aerothermodynamic loads and performance during high-speed flight and gas turbine operation. In the case of transonic airfoils, the occurrence of self-sustained shock wave oscillations, known as the *buffet* phenomenon (Lee 2001), adds further complexity.

For these reasons, SBLI has been one of the most important topic of research within the aeronautical scientific community over the past 70 years (Dolling 2001). Among others, Délery *et al.* (1986), Smits & Dussauge (2006), Doerffer *et al.* (2010) and Babinsky & Harvey (2011) represent the most notable reviews on this topic. Incident normal shock, oblique shock reflection, compression ramps and transonic airfoils were, and still are nowadays, typical geometries employed to explore this phenomenon.

Dolling (2001) reports that until the 1950s, SBLI were commonly described as relatively steady. Nowadays, it is now known that this description is incorrect, at least for separated turbulent interactions. Quantitative measurements of turbulent SBLIs reported a low frequency unsteadiness of the separation shock (Dolling & Murphy 1983; Erengil & Dolling 1991; Thomas *et al.* 1994). The two orders of magnitude separating the characteristic frequency of the incoming boundary layer from the frequency of the separation shock explain why the unsteadiness is classified as being low frequency, relative to the higher characteristic frequency of the incoming turbulent boundary layer. The work of Dupont *et al.* (2006) noted that the rear part of the interaction for an oblique reflected shock geometry also exhibits unsteadiness, which is in quasi-linear dependence with the reflected shock motion. The low frequency motion of the head shock, coupled to the expansion and contraction of the separated flow, is referred to as a *breathing* motion.

Whether discussing low-frequency unsteadiness or breathing motion, the necessity to find a consensus on the magnitude of the low frequency oscillations prompted a search for temporal scaling. Erengil & Dolling (1991) used the interaction length L_{int}, defined as the distance between the average position of the reflected shock and the extrapolation to the wall of the incident shock, and the upstream velocity U_∞ to scale the low-frequency unsteadiness. Based on this scaling, it was found in different experiments (Dussauge *et al.* 2006; Dupont *et al.* 2006; Ganapathisubramani *et al.* 2009; Souverein *et al.* 2009; Piponniau *et al.* 2009) and numerical investigations (Pirozzoli & Grasso 2006; Wu & Martin 2008; Touber & Sandham 2009; Priebe & Martín 2012) that the low-frequency oscillations in turbulent SBLIs falls in the range of Strouhal number $St = fL/U_\infty = 0.02 - 0.07$, where f is the frequency associated with the low frequency motion and L and U_∞ are as defined above. While the spatial and temporal dynamics of the global organisation of the flow have been illustrated (Dupont *et al.* 2006), and there is a clear comprehension of the qualitative mean flow organisation (Agostini *et al.* 2012), several mechanisms, sometimes conflicting, have been proposed to describe the mechanisms that govern the turbulent unsteady interaction.

The unsteadiness of reflected shocks has been commonly linked to turbulent structures within the incoming boundary layer (Erengil 1993). Early studies by Uenalmis & Dolling (1994) identified a connection between small-scale shock motions and turbulence fluctuations or velocity fluctuations in the boundary layer. Ganapathisubramani *et al.* (2007) later identified large-scale coherent structures, or superstructures, in the upstream boundary layer as responsible for low-frequency shock motion. Numerical simulations by Wu & Martin (2008) provided further insights, showing that the low-momentum structures of the incoming boundary layer and the separation point have a small correlation, indicating that the influence of the superstructures may be minimal. Additionally, it was found that both the shock motion and the motion of the separation point are correlated with the motion of the

reattachment point, suggesting that the downstream flow contributes to the low-frequency unsteadiness. Further research has indicated a potential role for downstream mechanisms. Touber & Sandham (2009) observed low-frequency unsteadiness even without upstream coherent structures, while Priebe *et al.* (2016) linked shock motion to downstream Görtler-like vortices. Another line of research has focused on the role of vortical structures emerging from the shear layer. Dussauge *et al.* (2006) suggested that the source of excitation of the shock motion can be attributed to eddies in the separated zone. Pirozzoli & Grasso (2006) found that eddies in the separated zone interact with the shock, producing acoustic waves that propagate upstream and induce a low-frequency oscillation in the shock, reminiscent of acoustic resonance seen in cavity flows. Piponniau *et al.* (2009) proposed a model that relates the mass recharge within the separated bubble to the flapping dynamics occurring near the reattachment point. The main parameter controlling the low-frequency shock motions is the spreading rate of the compressible mixing layer. Recent works, such as Chandola & Estruch-Samper (2017) and Jenquin & Narayanaswamy (2023), support the role of mass imbalance within the separated bubble, driven by shear layer entrainment, as the driving mechanism for the pulsation of the separated bubble. A more recent consensus suggests that both upstream and internal mechanisms contribute to low-frequency unsteadiness. The work of Puckett & Narayanaswamy (2024) suggests the combined effects of the separation bubble inherent unsteadiness and the shear layer instabilities as key contributors to the dynamics of swept SBLI. Thomas *et al.* (1994) and Dupont *et al.* (2006) observed strong coherence in pressure fluctuations near the separation bubble and reattachment point, indicative of a "breathing" mode of the separated region. Touber & Sandham (2011) extended this understanding by demonstrating that the interaction between the shock and boundary layer could be modelled as a first-order low-pass filter, implying that the low-frequency unsteadiness is an intrinsic property of the system. Clemens & Narayanaswamy (2014) proposed that while both upstream and internal mechanisms are always present, downstream effects dominate in strongly separated flows, with a combined mechanism prevailing in weaker separations.

It is evident that the focus of researchers has largely centered on turbulent interactions, with only recent efforts directed towards studying laminar and transitional SBLIs. Robinet (2007) conducted one of the earliest studies examining the temporal dynamics of laminar SBLI. In his work, both three-dimensional direct numerical simulations and linearised global stability analysis were carried out on an incident oblique shock impinging onto a laminar boundary layer. Simulations highlighted that for an increasing angle of the incident shock, the flow becomes three-dimensional, and the stability analysis revealed a bifurcation, generating the three-dimensional character of the flow. It was concluded that, beyond a critical angle of the incident shock wave, the two-dimensional and stationary flow becomes linearly globally unstable to a 3D stationary mode. However, Guiho *et al.* (2016) conducted a global stability analysis on a similar laminar interaction and found that the SBLI is globally stable for a wide range of flow parameters. They showed that unsteadiness is instead associated with non linear mechanisms between convective instabilities arising from the shear layer. The very recent study of Niessen *et al.* (2023) confirmed that the laminar SBLI they investigated cannot support the temporal growth of a disturbance in a fixed region of the space. Consequently, no two-dimensional global instabilities exist and thus all two-dimensional instability mechanisms are convective. They determined the most amplified perturbation content of SBLI in terms of the most amplified spanwise wavelength, which was found to be as large as 10% of the separated region, and frequency, about 9 kHz at the reattachment location. From these studies, it is clear that the low-frequency unsteadiness cannot be related to any unstable global mode.

Between the years 2012 and 2016, the European TFAST† project promoted several numerical simulations and experimental campaigns focused on transitional SBLI. This project permitted progress in understanding the role of transition in the context of the mutual interaction between the shock system and the laminar boundary layer. In particular, the DNS work of Sansica *et al.* (2014) studied the global response of the separated region to white noise forcing both upstream and inside the bubble. It was concluded that the internal forcing causes the low-frequency response near the separation point. This result is in agreement with Guiho *et al.* (2016), who showed that the low frequency response at the separation is more effective when the forcing comes from the recirculating region than when forcing the upstream boundary layer. Bugeat *et al.* (2022) suggested that the low-frequency dynamics of the SBLI corresponds to a forced damped stable mode, in which background perturbations through the receptivity mechanism continuously excite the flow. The flow thus behaves like a low-pass filter with respect to external disturbances.

To study the mechanism in more detail, Sansica *et al.* (2016) forced the inlet of the interaction with a pair of monochromatic oblique unstable modes. Despite the clean upstream condition, they observed low frequency unsteadiness near the separation point, with $St = 0.04$. They attributed the appearance of unsteadiness to the breakdown of the deterministic turbulence, leading to broadband pressure disturbances travelling upstream through the separated region (within the subsonic layer of the boundary layer) at phase velocity of $-0.6U_\infty$. The acoustic nature of the backward travelling pressure waves was challenged by Larchevêque (2016). In his study, fluidic backwards motion, with a possible origin at reattachment, was observed and the corresponding phase velocity, associated with low frequencies, was found to be of $-0.22U_\infty$. Bonne *et al.* (2019) conducted RANS based simulations coupled with a resolvent analysis and confirmed the backward motion of waves through the recirculating region. However, they suggested a density or acoustic nature of those waves. Moreover, the low frequency dynamics was described as a pseudo-resonance process that amplifies the instabilities in the separated shear layer and excites the shock foot, leading to the backward motion of density waves, with a phase velocity of $-0.1U_\infty$. A similar scenario of density disturbances propagating upstream through the recirculating region with a group velocity of $-0.18U_\infty$ was observed experimentally by Threadgill *et al.* (2021). Their detailed phase analysis of schlieren data permitted the identification of slow-moving density disturbances within the bubble that convect toward the shock foot and lead to the slow motion of the separation shock. Indeed, high-speed schlieren images showed that the separation shock exhibits low-frequency unsteadiness at $St = 0.025$. To the current authors' knowledge, this Strouhal value associated with the slow dynamics is the only one, in the context of the experiment, to be similar to those reported by numerical simulations.

Recent studies have suggested a non-linear mechanism as a possible explanation for the low-frequency unsteadiness. Sansica *et al.* (2014) noted that low-frequency unsteadiness occurs even without direct low-frequency forcing, and it is due to weak non-linear interactions with the shear layer instability modes. Mauriello *et al.* (2022) suggest that quadratic couplings between oblique modes are responsible for the oscillation of the reflected shock. The low frequency range in the separated region was found to be significantly quadratically coupled to the oblique mixing layer modes of much higher frequencies. They extended the analysis in the wavenumber space and showed that the flow features beneath the reflected shock, sustaining the low-frequency motion, are 2D. They also confirmed the existence of a slow upstream convective fluidic motion originating from the vicinity of the reattachment point. In their work, broadband and stochastic forcing was applied to stimulate the transition of the boundary layer to a turbulent state. Despite the non-forced transitional SBLI studied by Saïdi

† Transitional Location Effect on Shock Wave Boundary Layer Interaction

et al. (2025), similar strong triadic interactions were observed in the downstream region of the shock interaction playing a role in the low frequency dynamics. However, in all these studies the nature of the non-linearities that drives the unsteadiness remains unclear.

Building upon this body of work, the present work aims to investigate the presence of any unsteadiness and to address fundamental questions about the nature of nonlinearities in the context of the transitional SBLI. Motivated by the distinct approaches employed in prior researches, wherein Mauriello *et al.* (2022) work incorporated broadband forcing and Saïdi *et al.* (2025) study focused on a non-forced SBLI, the decision was to construct a simplified and didactic model. This model was designed to include a modal transition and enable precise control of the input parameters. Accordingly, one-period direct numerical simulations (DNS) combined with high-order statistical analysis have been performed on a $M = 1.5$ oblique shock reflection with separation. All details of the numerical setup and the flow conditions are given in Section 2. Starting from the work of Sansica *et al.* (2016), which suggests that the origin of the low-frequency unsteadiness is due to the breakdown into turbulence, deterministic simulations have been performed. The deterministic approach allows full control of the input conditions. We first reproduced the basic configuration used in the work of Sansica *et al.* (2016), where the incoming laminar boundary layer is stimulated with a pair of monochromatic oblique unstable modes. The result, presented in Section 3, showed that a pair of oblique unstable modes is not sufficient to produce the low frequency response of the head shock, although the breakdown to turbulence is observed to persist. Consequently, we have combined two different (in frequency) and opposite (in wavenumber) arrangements of unstable boundary layer modes. Our aim is to see if the introduction of nonlinearities triggers both the low frequency unsteadiness and the transition to turbulence in the boundary layer. Results are presented in Section 4. This deterministic approach, while providing valuable insights into the fundamental nonlinear interactions, inherently presents certain limitations. The use of specific monochromatic forcing arrangements represents a simplification of the broadband disturbances present in natural flows. Despite these limitations, this work addressed fundamental questions regarding the nature of nonlinearities driving low-frequency unsteadiness. In Section 5, we are interested in studying potential triadic interactions between the structures responsible for the boundary layer transition and those arising at the separation point. To achieve this, we have used high-order statistical tools. High-order spectral analysis is also used to identify the signature of low-frequency unsteadiness in wavenumber space. Two additional forcing configurations and a case with a different frequency combination are presented in Section 6. The concluding Section 7 summarises all the outcomes of this study.

It is essential to emphasise that this study focuses specifically on transitional SBLI. Relating the observed phenomena directly to turbulent SBLIs is challenging due to the fundamental differences in their spectral content and nature of the flows. Moreover, the deterministic approach allows for precise control and analysis of nonlinear interactions, but it also limits the direct extension to fully turbulent scenarios.

2. Flow conditions and numerical setup

2.1. *Numerical method and flow conditions*

The 3D compressible Navier-Stokes equations are solved in the conservative form, and are presented in the Cartesian coordinate system as

$$\frac{\partial \rho}{\partial t} + \frac{\partial \rho u_j}{\partial x_j} = 0 \qquad (2.1)$$

$$\frac{\partial \rho u_i}{\partial t} + \frac{\partial \rho u_i u_j}{\partial x_j} = -\frac{\partial p}{\partial x_i} + \frac{1}{Re}\frac{\partial \tau_{ij}}{\partial x_j} \qquad (2.2)$$

$$\frac{\partial \rho E}{\partial t} + \frac{\partial (\rho E + p) u_j}{\partial x_j} = \frac{1}{(\gamma - 1) RePrM_\infty^2} \frac{\partial}{\partial x_j}\left(\mu \frac{\partial T}{\partial x_j}\right) + \frac{1}{Re}\frac{\partial \tau_{ij} u_i}{\partial x_j} \qquad (2.3)$$

showing the non-dimensional form of the mass conservation equation, three momentum conservation equations, and the energy conservation equation, respectively. The indices i and j run from 1 to 3. In the equations, $\rho = \rho^*/\rho_\infty^*$ is the non-dimensional density, $u_1 = u = u^*/U_\infty^*$, $u_2 = v = v^*/U_\infty^*$ and $u_3 = w = w^*/U_\infty^*$ are the non-dimensional velocity components respectively in the x-, y- and z-directions scaled with free-stream velocity U_∞^*. $E = e + 1/2\rho(u^2 + v^2 + w^2)$ is the total energy per unit mass, with e as specific internal energy. The corresponding conservative variables are ρ, ρu, ρv, ρw, and ρE. The terms p, T are the non-dimensional pressure and temperature, respectively, while $\tau_{ij} = \mu\left[\partial u_i/\partial x_j + \partial u_j/\partial x_i - 2/3(\partial u_k/\partial x_k)\delta_{ij}\right]$ is the viscous stress tensor, where μ is the non-dimensional dynamic viscosity given by the Sutherland's law, with a Sutherland temperature of $T_S^* = 110.4K$, and δ_{ij} is the Kronecker delta function. The various physical variables are normalised using the corresponding free-stream values. However, pressure is normalised using the free-stream dynamic pressure term, $\rho_\infty^* U_\infty^{*2}$, i.e. $p = p^*/\rho_\infty^* U_\infty^{*2}$, while the unit total energy E is normalised by U_∞^{*2}. The dimensional quantities are denoted by a superscript *, which is dropped for non-dimensional quantities unless mentioned otherwise. Also, the subscript "∞" represents the free-stream conditions at the inflow. $x = x^*/\delta_{inlet}^*$, $y = y^*/\delta_{inlet}^*$ and $z = z^*/\delta_{inlet}^*$ are the non-dimensional coordinates scaled with the displacement thickness $\delta_{inlet}^* = 0.075$ [mm] at the inflow. The characteristic fluid dynamic time scale is $\delta_{inlet}^*/U_\infty^*$.

The *OpenSBLI* solver (Lusher *et al.* 2021), which is an open-source finite-difference-based solver, is used on structured Cartesian coordinate systems for the shock-reflection setup. A Local Lax-Friedrichs (LLF) flux splitting approach is used for the inviscid fluxes in characteristic space. Different variations of flux reconstruction schemes, *i.e.* WENO and TENO (Weighted and Targeted Essentially Non-Oscillatory), are available to compute the inviscid fluxes. As noted in earlier literature, the TENO scheme is less dissipative than the WENO schemes and hence, an adaptive version of 6th order TENO is used to perform the present simulations (Lusher *et al.* 2021). The viscous fluxes are computed using 4th order central differences, while a 3rd order Runge-Kutta scheme is used for time integration.

A 2D schematic of the computational setup is shown in Figure 1. The computational domain, marked with red dashed line, has extents $0 \leqslant x \leqslant 375, 0 \leqslant y \leqslant 140, 0 \leqslant z \leqslant 27.32$, and the number of points $(N_x, N_y, N_z) = (2050, 325, 200)$. The origin is located at the beginning of the computational domain. The grids are stretched in the wall-normal (y) direction using a tangent hyperbolic stretching function, while the grids are uniform in both streamwise (x) and spanwise (z) directions. All the distances are scaled with the displacement thickness $\delta_{inlet}^* = 0.075$ [mm] at the inflow plane, which is initialised using a similarity solution for a Mach 1.5 flow with a unit Reynolds number of 10^7 [m^{-1}]. Hence, the simulation Reynolds number based on this δ_{inlet}^* is $Re = 750$.

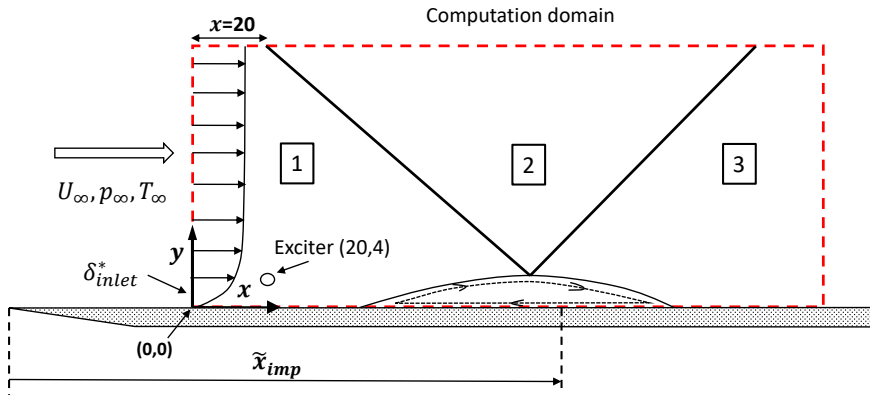The reference conditions are the same as Sansica *et al.* (2016), and Table 1 summarises

Figure 1: 2D schematic of the numerical setup, where the computational domain is demarcated with red dashed line.

M_∞	Re_{unit} [m^{-1}]	θ [deg]	P_∞ [Pa]	T_∞ [K]
1.5	1×10^7	2.5	2×10^3	202.17

Table 1: Aerodynamic flow conditions.

the aerodynamic parameters. At the wall, no-slip and isothermal boundary conditions (where the wall temperature is set to the laminar adiabatic wall temperature, i.e. $T_{wall} = T^*_{wall}/T^*_\infty \approx 1.381$) are used. Here, the reference free-stream temperature is $T^*_\infty = 202.17$ K. An extrapolation method is used at the inflow (for pressure) and outflow, while the span is periodic. The top boundary has shock jump conditions for a wedge-angle of 2.5° at $x = 20$, resulting in a pressure rise of $p_3/p_1 = 1.28$, where p_3 indicates the pressure state after the reflected shock. The Reynolds number at the location of inviscid shock impingement from the leading edge of the flat plate is $Re_{\tilde{x}_{imp}} = 1.95 \times 10^5$. These are further depicted in the schematic of the domain in Figure 1.

Disturbances are applied, upstream of the separation bubble, as a body-forcing term in the continuity equation, and a sample oblique wave representation with a particular frequency and spanwise wavenumber is given as

$$\rho'(x, y, z, t) = Real[A_0 \exp[-(x - x_c)^2 - (y - y_c)^2)] \exp[i(\pm\beta z - \omega t)]], \qquad (2.4)$$

A_0 in the above equation represents the amplitude of the forcing, while (x_c, y_c)=(20, 4) are the coordinates where the forcing is centered, which is roughly located at the edge of the shear layer. The forcing takes a maximum value at the central location and then tapers off in both x and y directions due to the first exponential term in (2.4). The last exponential term introduces variation in the spanwise and temporal dimensions, representing an oblique wave which travels at different angles with respect to the z-direction depending upon the + or - sign. The values of the spanwise wavenumber and circular frequency (β and ω respectively) are obtained from the linear stability theory (Sansica *et al.* 2016).

Various combinations of the simple deterministic forcing represented by (2.4) are used to trigger flow transition, the simplest of which is a pair of oblique waves with single circular frequency as used in Sansica *et al.* (2016). As the modifications represent a key point in this

286 study, an entire section (see Section 4) has been devoted to a comprehensive and detailed
287 treatment of them. At this point in the text it is important to emphasise that, when two
288 frequencies are forced, the combination is designed to be periodic over one cycle of the
289 difference frequency (i.e. $T = 2\pi/\Delta\omega$). This periodicity should be evident in the response
290 flow field under these forcings, and once this was ensured, the wall pressure data was collected
291 over one cycle of this difference frequency to evaluate the frequency spectrum.

2.2. *High-order analysis*

293 High-order spectra, corresponding to the Fourier transform of high-order correlation func-
294 tions, are the preferred tools to study non-linear interactions since they allow the analysis of
295 the quadratic couplings present in the governing Navier-Stokes equations on a scale-by-scale
296 basis.
297 One relevant high-order spectrum is the bispectrum (Tynan *et al.* 2001). It is formally
298 defined as the Fourier transform of the triple correlation, given by

$$Bis_{FGH}(\mathbf{x_F}, \mathbf{x_G}, \mathbf{x_H}, f_1, f_2) = \langle \hat{F}(\mathbf{x_F}, f_1) \ \hat{G}(\mathbf{x_G}, f_2) \ \hat{H}^*(\mathbf{x_H}, f_1 + f_2)\rangle \quad (2.5)$$

300 where $\langle\rangle$ denotes the averaging operation over time segments and possibly homogeneous
301 direction. $\hat{F}$, $\hat{G}$, and $\hat{H}$ are the temporal Fourier transforms at the locations $\mathbf{x_F}$, $\mathbf{x_G}$ and $\mathbf{x_H}$,
302 and the superscript * indicates the complex conjugate. The bispectrum reveals the energy
303 content associated with the cross-interaction between $\hat{F}$ and $\hat{G}$ ($\hat{F} \times \hat{G}$) and a third signal $\hat{H}$
304 at the frequency $f_1 + f_2$. This tool has been used extensively in the work of Mauriello (2024),
305 where a broadband stochastic forcing was used to stimulate the boundary layer transition
306 in the case of a transition SBLI at Mach 1.7. It has been proven to be very powerful in
307 highlighting the triadic interactions that occur between the oblique modes, i.e. the coherent
308 structures responsible for the transition to the turbulent state of the boundary layer, and the
309 structures of a 2D nature that emerge at the separation point. In the present work, the modal
310 transition has been fostered and a deterministic forcing has been applied (see Section 4),
311 plus the periodicity of the present simulations (one period simulation) imposes that, for the
312 lowest frequency $f_{min} = 1/T$, only a single segment, encompassing fully the period, can
313 be considered. It therefore excludes the possibility of averaging over segments leading to a
314 meaningless value of the normalised form of the bispectrum, i.e. the bicoherence ($Bic = 1$).
315 With this in mind, the bispectral analysis presented above is reformulated in term of spanwise
316 wavenumbers taking advantage of the time/space duality found for both the oblique mode and
317 the low-frequency unsteadiness (Mauriello 2024). This version of the bispectrum is given by

$$Bis_{FGH}\big((x_F, y_F), (x_G, y_G), (x_H, y_H), k_{z_1}, k_{z_2}\big) =$$
$$\langle \hat{F}\big((x_F, y_F), k_{z_1}, t\big) \ \hat{G}\big((x_G, y_G), k_{z_2}, t\big) \ \hat{H}^*\big((x_H, y_H), k_{z_1} + k_{z_2}, t\big)\rangle \quad (2.6)$$

319 where $\langle\rangle$ denotes a time average over one period. In this way, it is possible to de-
320 tect the wavenumbers responsible for non-linear interactions among the fixed locations
321 $(x_F, y_F), (x_G, y_G), (x_H, y_H)$. By time averaging in the wavenumber space, information about
322 the temporal behaviour is lost, but can be partially recovered by introducing a time delay τ.
323 The time delay can be introduced for the two time series F and G, consequently τ_1 and τ_2
324 identify the time lag occurring with respect to the third time series $H(f)$. The formula can
325 be written as

$$Bis_{FGH}\big((x_F, y_F), (x_G, y_G), (x_H, y_H), k_{z_1}, k_{z_2}, \tau_1, \tau_2\big) =$$
$$\langle \hat{F}\big((x_F, y_F), k_{z_1}, t + \tau_1\big) \ \hat{G}\big((x_G, y_G), k_{z_2}, t + \tau_2\big) \ \hat{H}^*\big((x_H, y_H), k_{z_1} + k_{z_2}, t\big)\rangle \quad (2.7)$$

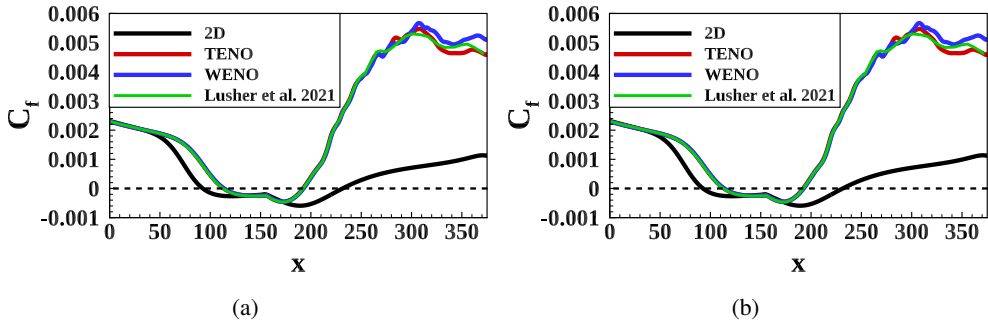327 In addition to the standard bispectrum maps defined in (2.7), optimal bispectrum maps can

Figure 2: Streamwise evolution of the friction coefficient C_f (a) and of the pressure at the wall normalised with the reference pressure P_{wall}/P_∞ (b).

be extracted. These maps are optimal in the sense that for all possible time delay pairs, the optimal time delay τ_{opt} is such that it maximises the bispectral energy content. For the sake of simplicity, the Fourier transforms $\hat{F}$, $\hat{G}$, and $\hat{H}$ will all be referred to by the letter G in the remainder of the text, and will be distinguished by subscript numbers running from 1 to 3.

3. Reference case of transitional SBLI

Sansica (2015) presented a detailed study using the local linear stability analysis, which identified the most unstable modes for the shock-reflection problem. Sansica *et al.* (2016) further performed DNS using these modes to perform the oblique mode transition using a pair of oblique modes to trigger transition. Lusher *et al.* (2021) used *OpenSBLI* solver to repeat these oblique mode transition simulations, however with different numerical methods and forcing setup. As we use *OpenSBLI* solver in the present research, we wanted to first cross validate our results against Lusher *et al.* (2021), starting with oblique mode transition, before performing more complicated forcing combinations that are further explored in this study. We next explain the validation results in this section.

The modal forcing is applied as a prescribed time-dependent forcing, where the density disturbances $\rho'(x, y, z, t)$ are superimposed on the density laminar flow field at $(x_c, y_c) = (20, 4)$. The values of the streamwise and spanwise wavenumbers (α and β respectively) as well as the pulsation frequency ω were extracted from the temporal stability map (see Figure 4.3 of Sansica (2015)). The spanwise width of the domain is set as $L_z = 2\pi/\beta$ such that it accommodates at least one wavelength of the most unstable oblique mode. Hence, the decision to set $L_z = 2\pi/\beta = \lambda_z = 27.32$.

The first set of simulations, that are performed using the deterministic forcing approach, use a pair of monochromatic oblique unstable modes, as used in Lusher *et al.* (2021) and Sansica *et al.* (2016), and the resultant forcing expression is given as

$$\rho'(x, y, z, t) = Real[A_0 \exp[-(x - x_c)^2 - (y - y_c)^2)] \ (e^{i(+\beta z - \omega t)} + e^{i(-\beta z - \omega t)})] \quad (3.1)$$

The oblique mode pair in the forcing expression uses $A_0 = 1.25 \times 10^{-3}$, $\beta = 0.23$ and a single frequency value of $\omega = 0.101$, similar to Sansica *et al.* (2016), to force the separated boundary layer. The *OpenSBLI* solver is used to run these simulations and the setup is identical to Lusher *et al.* (2021), except that we used a uniform grid in the streamwise direction. The aerodynamic conditions used in Lusher *et al.* (2021), including the freestream and shock jump conditions, and shock impingement location, are the same as Sansica *et al.* (2016). However, the present simulation is different from Sansica *et al.* (2016) due to the
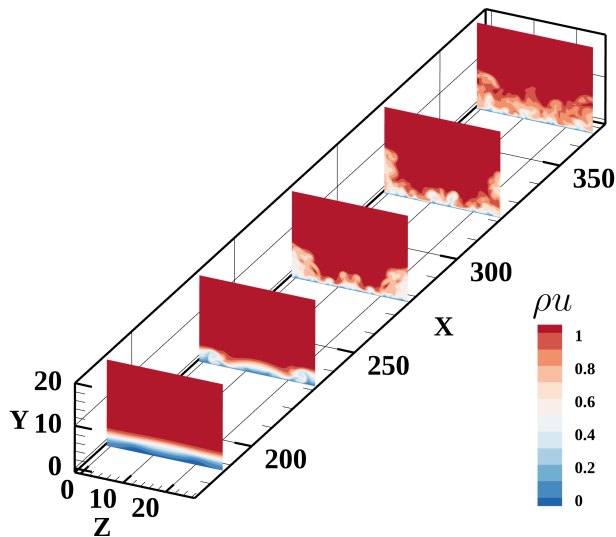
Figure 3: 3D view showing slices of ρu. The initial symmetry and its breakdown due to transition at downstream locations is showed.

360   way the forcing is applied. In the current simulations, the forcing is applied as a volumetric
361   forcing in the density term centered at $(x_c, y_c) = (20, 4)$, i.e. downstream of the inlet plane
362   and upstream of the separation bubble, while in Sansica *et al.* (2016), the forcing was applied
363   at the inflow in terms of the eigenfunctions for all conservative variables.

364   As we reran the setup of Lusher *et al.* (2021) with a uniform grid in the streamwise direction,
365   we performed some initial verification of our results against the skin friction results extracted
366   from the reference. Figure 2 (a) shows a comparison of skin friction from the rerun of Lusher
367   *et al.* (2021) setup with two different schemes, i.e. WENO and TENO. The 2D laminar skin
368   friction is also plotted for reference. It can be seen that the TENO version shows a slightly
369   better agreement with Lusher *et al.* (2021) compared to the WENO version. Some minor
370   deviations are noted towards the exit of the domain perhaps due to streamwise stretching used
371   in the reference simulation of Lusher *et al.* (2021). Figure 2 (b) shows minimal variations
372   of non-dimensional wall pressure, which is further non-dimensionalised with the reference
373   pressure $P_\infty = 1/\gamma M_\infty^2$ between the schemes. The 2D laminar wall pressure is also shown as
374   a reference.

375   A 3D visualisation of the flow is shown in Figure 3, which shows streamwise momentum
376   ρu at equally spaced x-y plane slices, with the first slice placed close to the reattachment
377   point at x $\approx$ 190. The second slice at $x \approx 230$ shows the first signs of spanwise non-uniformity
378   due to the production of streamwise vorticity. The spanwise symmetry starts to break once
379   further smaller scales are generated due to the transition to turbulence.

380   Figure 4 shows the spectral content of the pressure fluctuations at the wall in an x-f plane,
381   where x is the non-dimensional streamwise distance, shown in a linear scale, while f is the
382   non-dimensional frequency, shown with a logarithmic scale. The frequency is normalised
383   using the reference frequency scale $U_\infty^*/\delta_{inlet}^*$. In this way, the y-axis gives the Strouhal
384   number based on the length scale δ_{inlet}^*. It is worth mentioning that, unless explicitly stated
385   otherwise, the same normalisations (for x and f) will be applied to all the other spectra
386   presented in this study. The spectrum clearly shows the forcing $f = \omega/2\pi \approx 1.6 \times 10^{-2}$
387   introduced at $x = 20$. Its energy content extends over the whole domain and, starting
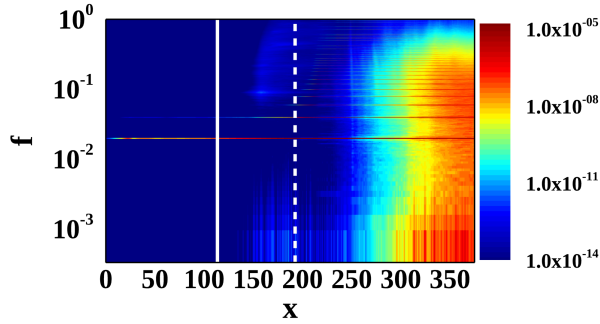388   from $x = 150$, subsequent harmonics develop towards increasingly higher frequencies. This

Figure 4: Power spectra spectrum of the wall pressure fluctuations for the case with a pair of monochromatic oblique unstable modes.

indicates that in the reattachment zone the boundary layer transitions to a turbulent state containing increasingly smaller structures (small scales) and increasingly higher frequencies. However, the separation point around $x = 110$ is free of any energy content, indicating that no low-frequency unsteadiness arises with this specific deterministic forcing.

The present power spectrum differs in one respect from Sansica *et al.* (2016), where weak low-frequency unsteadiness was identified using a local (in x) normalisation. Besides the difference in the normalisation, there are a few differences in methodology. In the current simulations, the perturbations are introduced as body forcing source term through the density equation downstream of the inflow plane, while in Sansica's case the forcing was applied at the inlet through the entire state vector. Also, the numerical method used in Sansica's case included a total variation diminishing (TVD) scheme (Sansica 2015) for shock capturing, while the present study uses a TENO scheme. On the hypothesis that the low-frequency content of the baseline case is sensitive to the numerical noise level, we prefer in the next section to introduce the nonlinearities in a deterministic way.

4. Deterministic forcing of low-frequency

The work of Mauriello *et al.* (2022) on a transitional SBLI similar to the present case highlighted the occurrence of triadic interactions between the unstable boundary layer modes and flow features of 2D nature emerging at the separation point. However, in their work, broadband and stochastic fluctuations were used as forcing, which prohibited the complete control of the inlet state of the flow. Nevertheless, according to their results, quadratic interactions are expected to occur, responsible for the low frequency unsteadiness phenomena. Considering the clean deterministic approach examined in the previous section, a second family of oblique modes was selected allowing the emergence of low-frequency content.

The choice was made to ensure that the frequency difference between these two wave families fell within the low-frequency range corresponding to the typical Strouhal number of the breathing phenomenon. Therefore, the pulsation frequencies ω_1 and ω_2 were chosen such that $\Delta\omega = \omega_2 - \omega_1$, where ω_1 was extracted from the stability analysis of Sansica *et al.* (2016) corresponding to the most unstable boundary layer mode, and $\Delta\omega = 2\pi\Delta f$. Δf was derived from the low-frequency Strouhal number $St_{LF} = 0.04$ found in the work of Sansica *et al.* (2016). Based on this, the two 3D waves families were selected such that

$$\rho_1'(x, y, z, t) = Real[A_0 \exp[-(x - x_c)^2 - (y - y_c)^2)]] \exp[i(\pm\beta z - \omega_1 t)]$$
$$\rho_2'(x, y, z, t) = Real[A_0 \exp[-(x - x_c)^2 - (y - y_c)^2)]] \exp[i(\pm\beta z - \omega_2 t)]$$

$$(4.1)$$

A_0	β	$\omega_1(f_1)$	$\omega_2(f_2)$	$\Delta\omega(\Delta f)$
1.25×10^{-3}	± 0.23	$0.1(0.0159)$	$0.104(0.0165)$	$0.004(0.0006)$

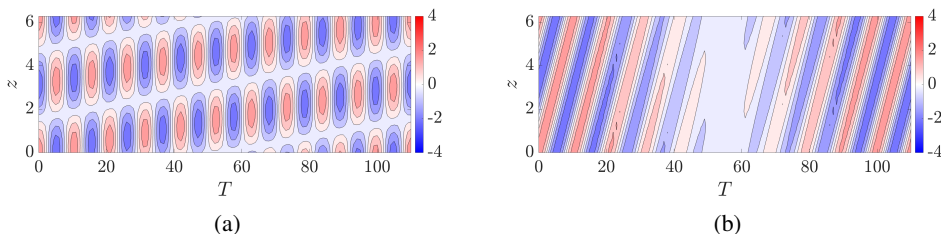Table 2: Unstable boundary layer waves characterisation.

Figure 5: Modal forcing combinations. Panel (a) is representative of the crossing waves family, and panel (b) is representative of the parallel beating waves family.

The sole distinction between the two families lies in their frequencies, with their spatial dimensions remaining unchanged as well as their initial level of energy A_0. Table 2 lists the values of the parameters extracted from the stability analysis (Sansica *et al.* 2016) and used to characterise the two 3D unstable wave families.

Various combinations of the most unstable mode waves are possible, two of which will be presented in this section, with more shown later (see Section 6). It is useful to establish the notation that will be used in the following sections before considering the first two wave combinations that were selected.

The general mathematical description of a family of oblique waves is given by equation (2.4). The formula shows that a family can include two waves of opposite spanwise wavenumber sign ($\pm\beta$). In a more physical sense, the expression represents two identical waves with the same magnitude of wavenumber vector $\mathbf{k} = \alpha\hat{i} \pm \beta\hat{k}$, but travelling at opposite angles concerning the streamwise flow progression. With this in mind, the superscript $^+$ denotes a set of waves distinguished by a positive wavenumber β, while the minus superscript $^-$ denotes the opposite waves. When waves of both families move in the same direction (same sign of β), we refer to them as a *parallel* family, while we use the terms *crossing* family when the spanwise wavenumbers are opposite. In addition, the subscript $_1$ indicates that the wave propagates with a characteristic frequency equal to the most unstable frequency determined by the stability analysis ($f_1 = \omega_1/2\pi$). The subscript $_2$ means that the characteristic frequency is set to $f_2 = \omega_2/2\pi$. According to this notation, the two combinations of 3D waves are given by

$$\text{Crossing waves: } \rho'(x, z, t) = \rho_1'^+(x, z, t) + \rho_2'^-(x, z, t)$$
$$\text{Parallel beating waves: } \rho'(x, z, t) = \rho_1'^+(x, z, t) + \rho_2'^+(x, z, t)$$

(4.2)

Figure 5 visualises the differences between the selected combinations for an illustrative case with $\omega_1 = 0.62$, $\omega_2 = 0.57$ and $\Delta\omega = 0.05$ given the period $T = 2\pi/\Delta\omega = 111$. If we exclude waves with negative β from the first family and waves with positive β from the second family, we generate what we called crossing modes, shown in Figure 5 (a). Conversely, by eliminating waves with negative spanwise wave numbers from this combination, we obtain an arrangement known as the parallel beating waves family, shown in Figure 5 (b).

The asymmetric combination of the two forcings is reflected in the organisation of the

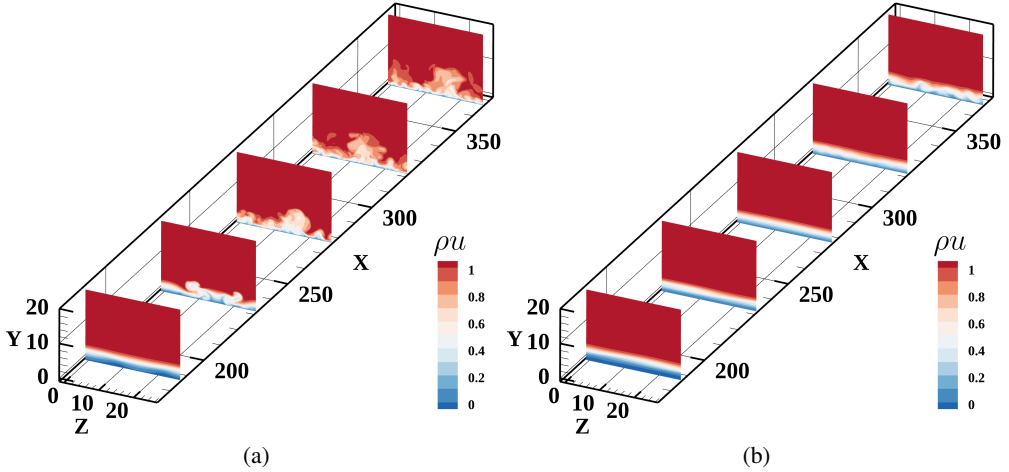Figure 6: 3D views of the flow field. Panel (a) is for crossing waves, and panel (b) is for parallel waves.

	Crossing waves	Parallel beating waves
A_0	2.5×10^{-5}	2.5×10^{-5}
L_{sep}	79	116

Table 3: Length (normalised by inlet displacement thickness) of the separated region for each combination of oblique mode waves. The maximum perturbation amplitude A_0 that is injected in each combination is shown.

flow, as can be seen in Figure 6. The 3D view of both flow fields is represented by five equally spaced slices. The contours show the streamwise momentum. Both flow fields show an incoming laminar boundary layer at the respective first slices. However, already at the location of the second slice, positioned at $x = 230$, the scenario starts to differ. In the case of crossing waves (panel (a)), the development of streamwise vortices is evident. They evolve in the streamwise direction, eventually leading to the transition of the boundary layer (see last slice). On the other hand, parallel beating waves develop smoothly and reach an incipient chaotic state only at the end of the computational domain. The nature of the boundary layer appears to be far from being fully turbulent.

Figure 7 plots the streamwise evolution of the friction coefficient for each family. The 2D laminar flow solution is also shown for ease of comparison. The black dashed horizontal line indicates $C_f = 0$, and helps to visualise the separated region. The extent of the separated zone is thus equal to the interval between the reattachment point x_R and the separation point x_S, such that

$$L_{sep} = x_R - x_S \qquad (4.3)$$

Table 3 summarises information about the flow reversal of each combination. It can be noted that both cases are injected with the same level of maximum perturbation amplitude, i.e. A_0, and hence are equivalent in terms of initial perturbation energy.

Both combinations reveal an incoming laminar boundary layer. As the shock system is approached, C_f departs from the laminar boundary layer branch. The boundary layer in the

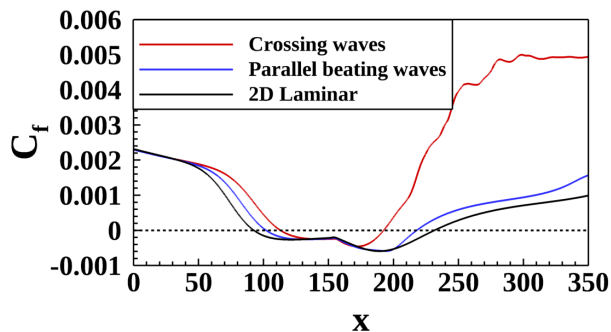Figure 7: Streamwise evolution of the friction coefficient for each oblique waves combination. The black dashed horizontal line indicates $C_f = 0$.
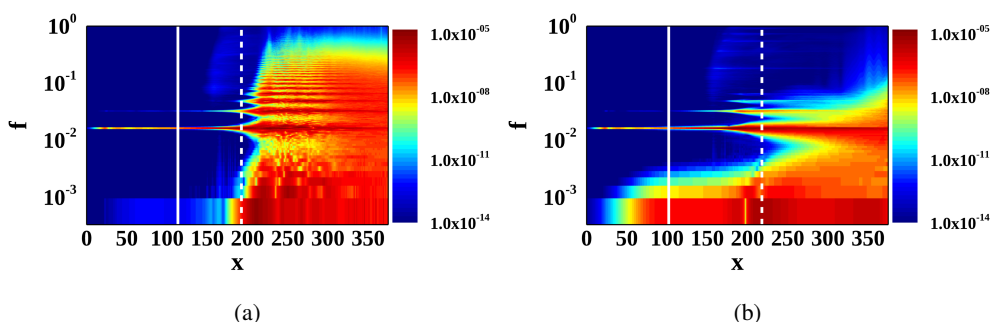

(a)

(b)

Figure 8: Power spectra of the wall pressure fluctuations for crossing waves (panel a) and parallel beating waves (panel b) families. In each spectra, the white solid vertical lines indicate the separation points, while the white dashed vertical lines indicate the reattachment points.

case of parallel beating waves separates further upstream than the crossing combination and reattaches further downstream, resulting in a longer separation bubble (see Table 3). The resulting boundary layer is far from turbulent indicating that this combination is much less efficient than the oblique mode transition mechanism that is active for crossing modes. This is in agreement with Mayer *et al.* (2011), who already observed that two oblique unstable waves with opposite wave angle can cause transition more rapidly than secondary instability. This also explains why the length of the reverse flow zone is longer for the parallel beating waves. In the case of crossing waves, although the energy level is the same as in the case of parallel beating waves, C_f keeps increasing and deviates from the laminar boundary layer trend.

Besides different lengths of the reversal region and the resulting downstream flow state, the two combinations of unstable boundary layer modes show a very different spectral response. Figure 8 shows the power spectrum of the pressure fluctuations field extracted at the wall for each family. In each spectrum, the white vertical lines indicate the separation (solid line) and reattachment (dashed line) points. All spectra clearly identify the forcing frequencies used upstream of the interaction. Note that two forcing frequencies have been applied, but from the spectra the distinction between them (a frequency difference of 0.0006) is barely visible and they appear as a single horizontal line.

A noticeable difference emerges when looking at the separation point. Parallel beating waves show intense activity at low frequency values, indicating that the head shock is
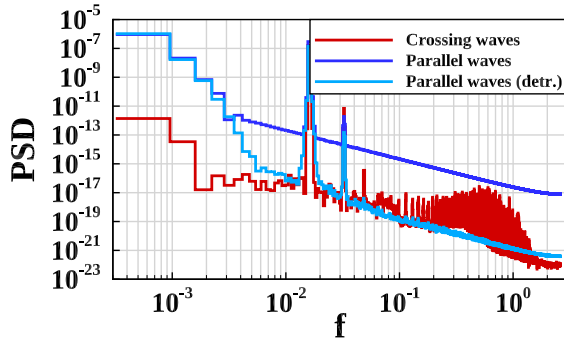
Figure 9: Power spectum extracted at the respective separation points for both crossing waves (red line) and parallel beating waves from raw (blue line) and detrended data using equation 4.4 (light blue line).

unsteady. This specific arrangement has hence allowed the breathing of the separated region. Although the same level of maximum perturbation energy is continuously added in both combinations, the crossing waves case lacks energy content at the separation point in the low frequency range.

If one looks at the region downstream of the reattachment point and frequencies higher than the forcing frequencies, the energy content for the crossing waves case shows a cascade towards its harmonics and begins to fill the spectrum up to high frequencies representing the characteristics of turbulence. This cascading process is almost absent in the parallel family case (see panel (b) of Figure 8) and is consistent with the result that we saw earlier from the skin friction profile variation for the two cases.

Figure 9 shows the evolution of the amplitude of the power spectrum for pressure fluctuations at the wall extracted at the respective separation points for both families. Both the x and y axes are plotted on a logarithmic scale and show a power-law trend. Note that the spectrum of the parallel case exhibits a -2 power law beyond the very low frequency range (dark blue line). This can be associated with the Fourier series of a sawtooth wave. This means that the dynamics at the separation point deviates from a strictly periodic behavior due a small linear drift. All the flows considered in this study which are associated with a low-frequency dynamics in the vicinity of the separation point, are subject to such drifts. However their amplitude is decreasing from period to period (results not shown). All computations have therefore been extended in time up until the extrapolation of the -2 power law down to the lowest frequency is at least four orders of magnitude lower than the natural energy content for that frequency. This ensures that the jump associated with the lack of periodicity is equal to at most 3% of the peak-to-peak amplitude of the low-frequency fluctuation. In order to unveil the high-frequency behavior of the flow in all subsequent analyses that involve in some way the time-Fourier space, the drift is removed by detrending the data in such a way that the C^0 continuity of the variable is ensured through the periodicity:

$$\rho_w^d (x, z, t) = \rho_w (x, z, t) + \frac{t - t_0}{T} \left\langle \rho_w (x, z, t_0) - \rho_w (x, z, t_0 + T) \right\rangle_z \qquad (4.4)$$

where $\langle \rangle_z$ is the averaging operator in the spanwise direction. The rationale behind the detrend scheme built from the spanwise average of the jump induced by periodicity is that discontinuities identified in the separated region are mostly associated with flow features of 2D nature (Mauriello 2024). They have in fact a Fourier series expansion in the spanwise direction fully dominated by the $k_z = 0$ coefficient. Because of the average, the correction

	Crossing waves	Parallel beating waves
L_{int}	46.5	58
L_{sep}	79.0	116
$St_{L_{int}}$	–	0.037
$St_{L_{sep}}$	–	0.074

Table 4: Interaction and separation lengths (normalised by inlet boundary layer thickness) and the corresponding Strouhal number for both families of crossing and parallel beating waves.

tends to zero in the non-deterministic region of the flow, where periodicity is not expected, and therefore should not be enforced.

It can be seen in Figure 9 that this correction removes the -2 power law and that the corrected spectrum (light blue line) shows no significant higher-order power law, confirming the linear nature of the drift. Analyses described in the following sections which do not involve moving to the frequency space, were performed on both the raw and detrended data. No significant differences were found between the two approaches, even when considering early periodic datasets with 10 times greater drifts. Therefore, for simplicity and consitency, it was decided to present the metrics obtained from the detrended data only.

In the case of parallel waves (using the linear detrended data), the order of magnitude at low frequency is approximately $O(10^{-6})$. In the case of crossing waves, the order of magnitude is approximately $O(10^{-12})$, for which the interaction is steady. The profiles show a constant decrease and both peak at the forcing frequencies. Moreover, both cases show an additional peak corresponding to the first harmonic. This result suggests that nonlinear interactions are already at play at the separation point. From this analysis, we can infer that the distinctive combination of oblique mode families, for the same magnitude of the perturbation energy, is the predominant factor influencing the low frequency behaviour of the head shock.

In the framework of turbulent SBLI, various numerical and experimental studies have shown that there is a consistent collapse of the magnitude of the low-frequency oscillations when the corresponding frequency is scaled with the interaction length L_{int}, defined as the distance between the average position of the reflected shock x_{int} and the extrapolation to the wall of the incident shock x_{imp}. The resulting Strouhal number is thus $St_{L_{int}} = f L_{int}$ where both f and L_{int} are non-dimensional quantities normalised using reference frequency $U_\infty^*/\delta_{inlet}^*$ and δ_{inlet}^*, respectively. On the basis of this scaling, the literature indicates that the low-frequency oscillations in turbulent SBLI fall in the $0.02 - 0.07$ range of Strouhal number. However, the length of the separation bubble L_{sep}, defined as the distance between the separation point x_S and the reattachment point x_R (see equation 4.3), can also be used as a length scale and hence $St_{L_{sep}} = f L_{sep}$ (same as Sansica *et al.* (2016)). Although the correct length scale remains unclear, including whether the same scaling can be applied in the case of transitional SBLI, a compilation of the different lengths and the corresponding Strouhal number are provided in Table 4. Since only the arrangement of parallel beating waves led to an unsteady interaction, the Strouhal number is presented solely for this case.

5. Quadratic couplings

The spectral analysis of the pressure fluctuations at the wall in the previous section showed an approximately steady interaction (lacking the low-frequency content) in the case of the crossing family, while an unsteady interaction was found for the parallel arrangement. This

Quadratic couplings	Resulting quadratic couplings
$(-\omega_1, +\beta) \times (-\omega_2, -\beta)$	$[(-\omega_1 - \omega_2), 0]$
$(-\omega_1, +\beta) \times (-\omega_2, -\beta)^*$	$[(-\omega_1 + \omega_2), 2\beta]$
$(-\omega_1, +\beta)^* \times (-\omega_2, -\beta)$	$[(\omega_1 - \omega_2), -2\beta]$
$(-\omega_1, +\beta)^* \times (-\omega_2, -\beta)^*$	$[(\omega_1 + \omega_2), 0]$

Table 5: Frequency-wavenumber combinations of Fourier modes for the crossing wave case. Symbol * indicates the complex conjugate. The first column shows the possible combinations in compact notation; the second column shows the resulting combinations after multiplication.

raises the question: how can the influence of specific arrangements of oblique modes on the interaction be explained?

The analysis stems from mathematical considerations starting from the perturbation field described by *ansatz* (2.4). It is a normal mode reduction and the Fourier transform allows for the identification of frequencies within the original signal. For a single oblique travelling wave in physical space with $(-\omega, +\beta)$, the *ansatz* (2.4) in the Fourier space can be expressed in a compact notation as

$$(-\omega, +\beta) \quad \text{and} \quad (+\omega, -\beta) \tag{5.1}$$

where $\omega = 2\pi f$ is the circular frequency, and $\beta = 2\pi/\lambda_z = 2\pi/L_z$, as there is a single wavelength in the spanwise domain length of L_z. Hence, the wave velocity is related to the spanwise wavelength λ_z and frequency f as $c_z = \omega/\beta$ or $\lambda_z f$. Note that because the Fourier transform is applied to real data, Hermitian symmetry holds and each signal in spectral space is supported by its complex conjugate (c.c.), shown in the second bracket in equation (5.1).

Fourier modes of different signals can be quadratically combined with each other, resulting in new modes that are included in the new signal. Recalling that in the case of crossing waves two families of oblique modes are included (see equation (4.2)), in the frequency-wavenumber notation they read $[(-\omega_1, +\beta)+\text{c.c.}]\times[(-\omega_2, -\beta)+\text{c.c.}]$. Table 5 shows all possible frequency-wavenumber quadratic combinations, specifically the first column presents the product of various possible combinations for quadratic interactions of modes, while the second column shows the corresponding resulting quadratic combinations after multiplication.

At this point, it is important to emphasise that our main focus is on the low frequency unsteadiness that affects the separation point. Consequently, when examining the interactions between crossing waves, we limit our attention to combinations that result in a positive difference between the frequencies, i.e. $(\omega_2 - \omega_1)$. For crossing waves, the only combination that respects this condition gives $[(\omega_2 - \omega_1), 2\beta]$, i.e.

$$\omega_{LF} = \omega_2 - \omega_1 \longrightarrow \beta + \beta = 2\beta \tag{5.2}$$

Note that also the combination resulting in $(\omega_1 - \omega_2)$ is present. This is the Hermitian symmetric counterpart of $(\omega_2 - \omega_1)$ that is required to reconstruct the real-valued function that mathematically describes the oblique modes (see *ansatz* (2.4)). However, it yields negative frequencies, and in this context, we only consider resulting frequencies that are positive, hence $(\omega_2 - \omega_1)$. Therefore, in the graphical representation of the forthcoming results, only the positive frequency space (i.e. half plane) is presented.

One can note that this low frequency combination for the crossing waves case results in

	Low frequency		High frequency	
	$(\omega_2 - \omega_1)$	k_{LF}	$(\omega_2 + \omega_1)$	k_{HF}
Crossing waves:				
$(-\omega_1, \beta) \times (-\omega_2, -\beta)$	$\beta + \beta = 2\beta$	2	$\beta - \beta = 0$	0
Parallel beating waves:				
$(-\omega_1, \beta) \times (-\omega_2, \beta)$	$\beta - \beta = 0$	0	$-\beta - \beta = -2\beta$	-2

Table 6: Summary of the quadratic couplings for the modal forcing combinations. The subscripts "$_{LF}$" and "$_{HF}$" in k indicate the low-frequency dynamics $(\omega_2 - \omega_1)$ and the high-frequency dynamics $(\omega_2 + \omega_1)$ respectively.

a non-zero resultant spanwise wavenumber ($k_{LF} \neq 0$), implying that the associated flow features are 3D in nature. The work of Mauriello (2024) on a transitional SBLI showed that the low-frequency unsteadiness is driven by structures populating the foot of the head shock, whose nature is 2D in wavenumber space and they result from quadratic interactions. Based on this result, it can be explained why crossing waves only lead to a steady interaction.

By following the same mathematical approach for the parallel beating waves, we obtain

$$\omega_{LF} = \omega_2 - \omega_1 \longrightarrow \beta - \beta = 0 \tag{5.3}$$

The resultant spanwise wavenumber in the low-frequency range is therefore $k_{LF} = 0$, and low-frequency unsteadiness are observed for such a case.

Table 6 summarises all possible combinations at both low frequency $(\omega_2 - \omega_1)$ and high frequency $(\omega_2 + \omega_1)$ for each family of oblique modes. The resultant spanwise wavenumber corresponding to the low frequency (high frequency) quadratic coupling is also presented as k_{LF} (k_{HF}), which highlights the 2D or 3D nature of the flow features. Note that for each family, its definition in the frequency-wavenumber space is presented, omitting its complex conjugate part. When the parallel combination is active in the low frequency range, the topology of the flow is two-dimensional in the wavenumber space, with $k_{LF} = 0$. Conversely, when dealing with high frequency $(\omega_2 + \omega_1)$, a different scenario emerges, with crossing waves responsible for a 2D periodicity of the flow.

5.1. *Frequency, wavenumber, and location*

More information about the interactions can be obtained from a spectral analysis of the resulting flow. Figure 10 displays the power spectrum of wall pressure fluctuations in the spanwise wavenumber domain, at fixed frequencies and for each combination of oblique waves. The wavenumber is presented as a multiple of the imposed wavenumber β in the form $k = k_z/\beta$. This approach enables a direct comparison of the results with the theoretical ones presented in Table 6. The white vertical lines indicate the position of the separation point (solid line) and the reattachment point (dashed line) respectively. For simplicity, we will use frequency f instead of circular frequency ω. Consequently, the left column plots the flow organisation in the low frequency dynamics $(f_2 - f_1)$, while the right column shows the space arrangement for $(f_2 + f_1)$. Furthermore, the first row illustrates the results for the crossing family (a)-(b), while the second row shows the parallel beating family (c)-(d).

In the high-frequency dynamics (right column), the crossing combination of waves gives rise to two-dimensional waves $k = 0$, originating around the reattachment point and extending downstream. However, a similar downstream contribution at $k = 0$ is absent for the parallel
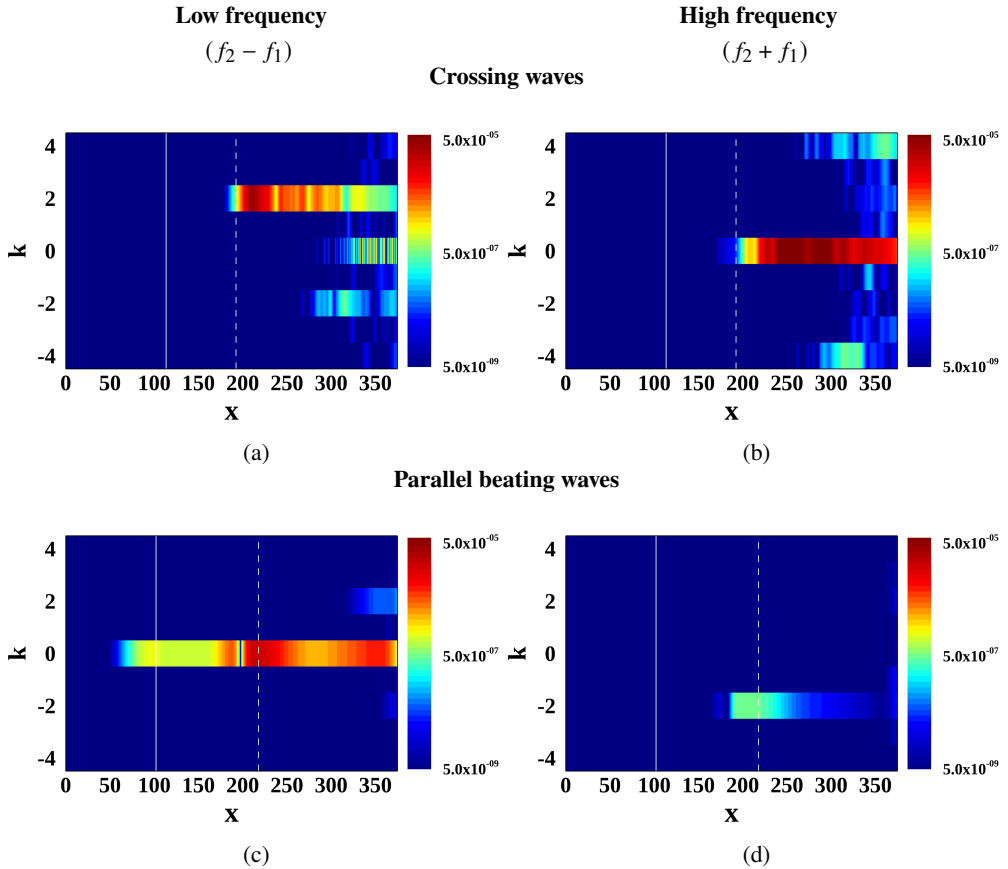
Figure 10: Streamwise distribution of the power spectra for each normalised wavenumber at selected frequencies: left column indicates low frequency ($f_2 - f_1$), right column indicates high frequency ($f_2 + f_1$). The white vertical lines indicate the position of the separation point (solid pattern) and the reattachment point (dashed pattern) respectively. Panels (a)-(b): crossing waves; panels (c)-(d): parallel beating waves.

beating family at high frequency ($f_2 + f_1$) (see panel (d)). This region is populated by three-dimensional structures whose value of k is equal to -2.

A detailed examination of the slow dynamics (left column) reveals that only the parallel combination (see panel (c)) leads to two-dimensional structures, originating before the separation point. Conversely, in the case of crossing waves, the spectral content for two-dimensional structures does not emerge at this same location, thereby confirming their absence in the slow dynamics at the separation point. These observations are consistent with the findings of the previous section, i.e. that the appearance of low-frequency unsteadiness only occurs for wavenumber combinations that are 2D.

5.2. *Non-linear analysis in terms of wavenumber*

The previous subsection showed that oblique mode families interact in such a way as to produce two- and three-dimensional flow features at specific locations in both slow and fast dynamics. Exploiting the periodicity of the present simulation (one-period of the difference mode $\Delta\omega$), the extended version of the higher-order spectral analysis, as presented in Section 2.2, is applied in order to detect any possible triadic interactions. In addition, a further

simplification has been introduced. In the study of Mauriello *et al.* (2022) it was observed from bicorrelation maps that the quadratic interactions between oblique modes are maximal for null time-delay between the modes (see Figure 8 of their paper, high bispectral content is observed along the diagonal shown in the bispectrum map). In short, for a time $\tau_1 = \tau_2 = \tau$, the nonlinear interaction between oblique modes is at its maximum energy activity. Consequently, the same time delay $\tau_1 = \tau_2$ is set for the source sensors used to extract possible quadratic couplings between oblique modes with respect to the target sensor. Using these assumptions, the equation (2.7) is reduced to

$$Bis_{FGH}\big((x_F, y_F), (x_G, y_G), (x_H, y_H), k_{z_1}, k_{z_2}, \tau\big) =$$
$$\langle \hat{F}\big((x_F, y_F), k_{z_1}, t + \tau\big) \, \hat{G}\big((x_G, y_G), k_{z_2}, t + \tau\big) \, \hat{H}^*\big((x_H, y_H), k_{z_1} + k_{z_2}, t\big)\rangle \tag{5.4}$$

Optimal bispectral maps are presented in this section. The optimality results from the time delay τ_{opt}, which maximises $Bis_{F,G,H}(k_{z_1}, k_{z_2}, \tau)$. For the sake of simplicity, we will drop the subscript "z" in the wavenumber k, and the three signals will all be denoted by the sole letter G. Subscripts from 1 to 3 are used to distinguish the signals. The first two signals G_1 and G_2 have been chosen as source signals and are located between the forcing location and the separation point at $x = 45$. At this location the spectral decomposition of the wall pressure fluctuations has the same power content in each of the cases (see Figure 8) and the flow field in this region is described solely by the dynamics of the oblique modes. This implies full knowledge of the power contribution of the source sensors G_1 and G_2, which is the same for both families. Consequently, it is natural that the target sensor G_3 (located either at the separation or at the reattachment points) will have a power contribution that depends only on the power due to the quadratic couplings, which varies according to the case under consideration. An alternative approach would be to use the bicoherence to quantify the level of nonlinear coupling. However, in the latter case, the normalisation used to define the bicoherence yields a measure of the strength of the quadratic coupling regardless of the level of quadratic power involved, thus highlighting a set of quadratic couplings that have no dynamical impact due to negligible energy content. In contrast, the norm of the bispectrum directly reveals the energy content associated with the nonlinear couplings. The location of the three sensors is the same for all further analyses, unless clearly stated.

Figure 11 shows maps of the norm of the optimal bispectrum for each oblique mode combination. In all maps, the two source sensors G_1 and G_2 are located at $x = 45$ for the reason previously explained, whereas the destination sensor G_3 is located either at the separation point (left column) and at the reattachment point (right column). This approach allows the 2D and/or 3D nature of the flow features responsible for the non-linear coupling between the upstream region and the separation and reattachment locations to be highlighted. Note that the spanwise wavenumbers are presented with subscripts $_1$ and $_2$ to indicate that the quadratic couplings result from all possible wavenumbers detected by sensor G_1, i.e. k_1 and G_2, i.e. k_2. Also note that (k_1, k_2) pairs resulting in squared bicoherence values higher than 0.25 are encircled by a black thick line in order to demarcate couplings effectively resulting in a high level of *relative* quadratic power.

When considering the crossing waves combination at the separation point (see panel (a)), the set of wavenumbers resulting from quadratic non-linearities of the oblique modes are dominated by couplings involving at least one oblique mode, i.e. $k_{1,2} = \pm 1$, all with a similar amount of quadratic power (orange circles). In contrast, for the parallel wave case, the bispectral map is dominated by the combination $(k_1, k_2) = (-1, 1)$, for which the level of bispectral content is higher (see panel (c)). This means that quadratic couplings at the separation point lead to 2D flow features with $k_3 = k_1 + k_2 = 0$. However, it is evident that
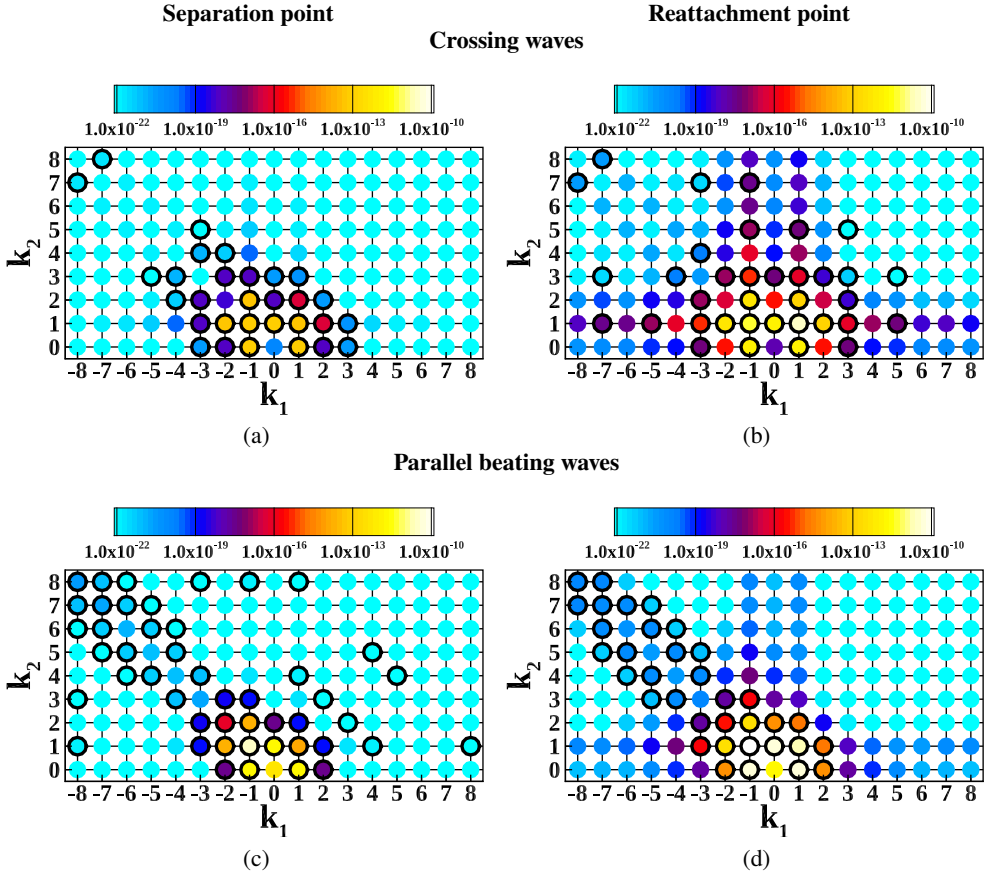
Figure 11: Modal forcing: maps of the norm of the optimal wavenumber bispectrum, with pairs resulting in bicoherence value higher than 0.25 encircled in black. Left column: the target sensor G_3 is located at the separation point; right column: the target sensor G_3 is located at the reattachment point. Panels (a)-(b): crossing waves; panels (c)-(d): parallel beating waves. All maps show quadratic interactions with the two source sensors $G_1 = G_2$ located at $x = 45$.

685 2D quadratic combinations also appear for the subsequent $k_2 = -k_1$ couplings visible along
686 the diagonal, despite the decrease in the bispectral power content. Nevertheless, at this stage
687 of the analysis, it is still not possible to infer whether the quadratic interactions arise from
688 the interaction of the oblique modes after they have passed through the shock interaction
689 system and thus have the possibility of flowing back through the separated region, or whether
690 they are the beginning of pure triadic interactions that are about to develop and will continue
691 to develop along the shear layer. Another important difference between crossing waves and
692 parallel beating waves, when observed at the separation point, is the resulting non-linear
693 contribution introduced to the mean field $(k_1, k_2) = (0, 0)$ that occurs in the case of the
694 combination of parallel waves. This non-linear modulation of the mean field is also present,
695 for this particular combination, when the target sensor is positioned at the reattachment point
696 (see panel (d)). However, the corresponding level of the bicoherence is low, indicating that
697 the power issued from this coupling only contributed to a small amount of the total power at
698 $k_3 = 0$.
699   On the other hand, strong quadratic couplings for all integer multiples of the fundamental
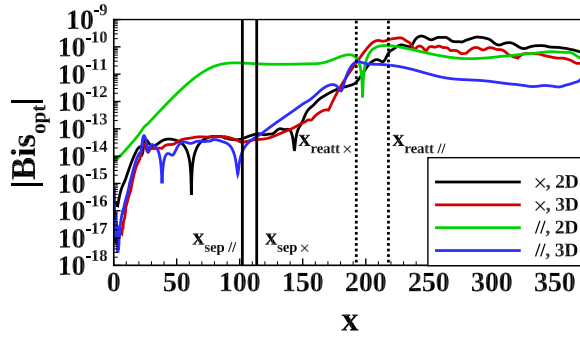
Figure 12: Norm of the optimal wavenumber bispectrum for both crossing (×) and parallel beating (//) waves extracted for the resulting 2D ($k_3 = 0$) and 3D ($k_3 = 2$) flow characteristics.The vertical black lines indicate the separation (solid) and reattachment (dashed) points.

700 wavenumber $k_{1,2} = 1$ appear for the crossing wave family at the reattachment point (see
701 panel (b)). The oblique modes at the reattachment region interact nonlinearly, initiating the
702 cascade process towards higher wavenumbers (smaller scales) typical of the turbulent kinetic
703 energy cascade. For small $k_{1,2}$, the same organisation of the quadratic power is observed as
704 for the separation point. The combination of $k_{1,2} = 1$ is largest, indicating a direct quadratic
705 interaction between oblique modes resulting in a 3D organisation of the flow.

706 When restricted to the reattachment point, the parallel waves show a cascade process
707 towards higher $k_{1,2}$ that is at its early stages, as only a few cascading combinations of the
708 fundamental harmonic are visible (see panel (d)). These results support the previous finding
709 that the crossing arrangement is more prone to turbulence breakdown than the parallel wave
710 arrangement.

711 Limiting attention to combinations of 2D (($k_1, k_2) = (-1, +1)$) and 3D (($k_1, k_2) =$
712 $(+1, +1)$) wavenumbers from the previous maps, information on the streamwise evolution
713 of the norm of the optimal bispectrum is extracted and presented in Figure 12. Note that
714 in this figure, the target sensor G_3 is no longer limited to the two locations of separation
715 and reattachment, but extracts information for each point in the x direction. For the clarity
716 of the figure, the crossing waves are indicated in the legend by the symbol ×, while the
717 parallel beating family is indicated by //. The vertical black lines indicate the separation
718 (solid line) and reattachment (dashed line) locations for each wave family. A high value of
719 the optimal bispectral content is observed in the separated flow region for the oblique mode
720 coupling resulting in 2D spanwise organisation of the flow in the case of parallel beating
721 waves, confirming that most of the quadratic couplings result in $k_3 = 0$ (see green line) for
722 such an arrangement. In the same region, nonlinear couplings between the oblique modes
723 resulting in 3D (parallel beating waves) and 2D and 3D (crossing waves) flow characteristics
724 begin to develop within the separation bubble. After the shock interaction, quadratic couplings
725 saturate, with significantly higher plateau levels in the case of the crossing waves, especially if
726 3D interactions ($k_3 = 2$) are considered. Those associated with the occurrence of the turbulent
727 energy cascade dominate, confirming the occurrence of the turbulent energy cascade, which
728 is observed to be less pronounced in the case of parallel beating waves for $k_3 = 2$.

729 The norm of the optimal bispectrum does not directly indicate the frequency range in which
730 the quadratic couplings occur. In this context, the time-filtered optimal bispectral maps are
731 computed. They are obtained by bandpass filtering in time the target signal $G_3(k_1 + k_2, t - \tau)$.
732 The filter retains either the frequencies associated with the low-frequency dynamics ($f_2 - f_1$)
733 or those associated with the high-frequency dynamics ($f_2 + f_1$). This enables the whole

frequency spectrum used to calculate the optimal bispectral power to distinguish whether the predominant contribution comes from quadratic interactions occurring at low or high frequencies. In each plot of Figure 13, the separation (solid line) and reattachment (dashed line) locations are shown to ease visualisation of the separated region. In addition, the colour code uses black for the unfiltered target signal G_3, red for low-pass filtering, and blue for all signals that retain only the high-frequency range. The total frequency spectrum for the 2D periodicity in the case of the crossing arrangement (see panel (a)) is fully dominated by quadratic couplings occurring at high frequency ($f_2 + f_1$), and the contribution of nonlinear couplings at low frequency is marginal. The opposite situation is observed for the same 2D organisation of the flow in the case of parallel beating waves (see panel (c)). Most of the nonlinear interaction is detected in the low frequency range (see the red diamonds overlapping the black line). The high value of the optimal bispectral content through the separated region again supports the observation that non-linear coupling due to oblique modes in the specific case of parallel arrangement is responsible for the appearance of 2D flow features at the separation point. These flow features are in turn sustaining the low frequency motion of the head shock. In short, in the wavenumber space, the trace of the low-frequency unsteadiness is two-dimensional. Indeed, for the crossing waves with periodicity $k_3 = 0$, only quadratic couplings acting at high frequency are observed, and in Section 4 we have observed that in such a case the interaction is steady. The three-dimensional periodicity requires careful analysis, as the quadratic couplings also take into account beatings of a different nature. Although most of the contribution to the total bispectral content comes from the low-frequency (crossing waves) and high-frequency (parallel beating waves), a complete overlap of the plots is not observed. The full bispectral power is only recovered when the self-quadratic coupling of each single oblique mode is taken into account, i.e. $f_1 + f_1 = 2f_1$ and $f_2 + f_2 = 2f_2$ in the frequency range that best maximises the total quadratic power. This is shown in panels (b) and (d) with the green diamond symbols.

5.3. *The direction of quadratic couplings*

Information on the directionality of the quadratic motion can be extracted by mapping the norm of the bispectrum into the time delay-space domain, as in Figure 14. The contours represent the norm of the bispectral power, and information on the time periodicity and direction of the motion is available from its pattern and the slope associated with it. Note that the contours are saturated such that low amplitude activity can be highlighted. The inverse of the ratio of τ to x directly gives the value of a propagation velocity associated with the quadratic coupling under consideration, normalised with the external velocity, i.e. U_B/U_∞. In each map, the location of the separation and reattachment points is indicated by black vertical lines, solid for the former and dashed for the latter. Propagation velocities deduced from the map in various regions of the flow thus delineated are listed in Table 7. Note that the streamwise evolution has been divided into three regions: from the forcing location ($x_{forcing} = 20$) to the separation point, within the recirculating region and downstream the reattachment point.

Downstream motion is observed for crossing waves, regardless of the 2D (see panel (a)) or 3D (see panel (b)) nature of the flow structures. However, the fundamental periodicity is different. A short period corresponding to $T = 1/(f_1 + f_2)$ is observed for $k_3 = 0$. This result is consistent with the previous observations, for which most of the quadratic activity concerns the high frequency range of the total spectrum (see panel (a) of Figure 13).

Indeed, the upstream region of the flow is dominated by slow periodic dynamics corresponding to $T = 1/(f_2 - f_1)$, in agreement with the results presented in the previous section (see panel (b) of Figure 13). But, as seen in this plot, there are also quadratic couplings of lower amplitude associated with self-interactions of oblique modes towards frequencies
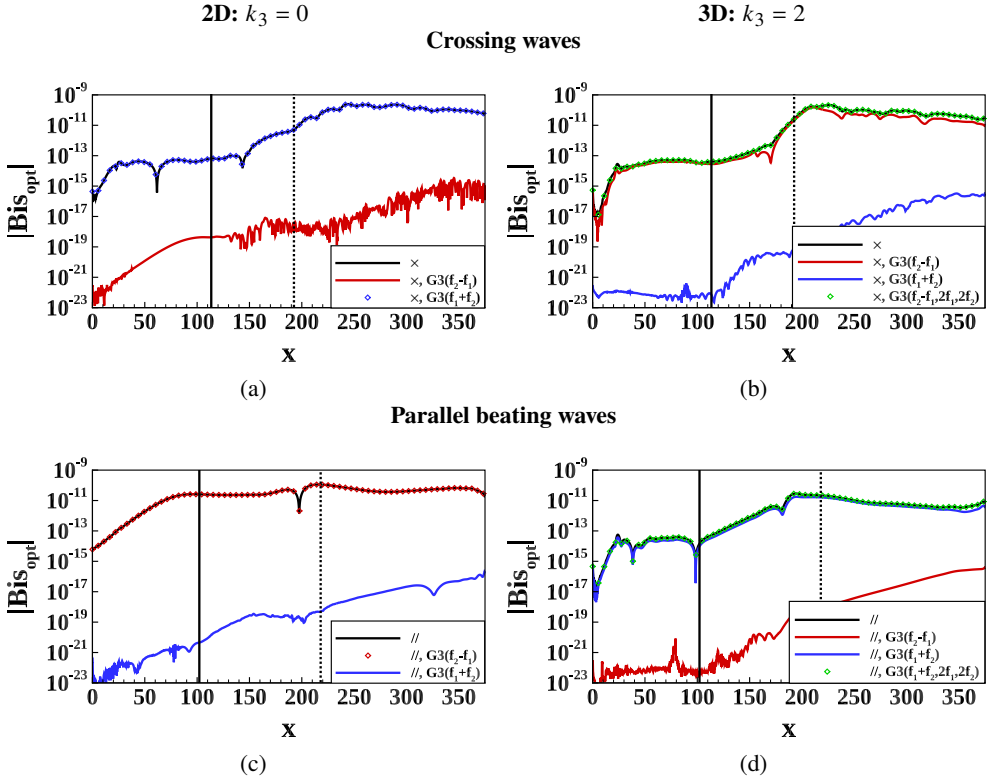
2D: $k_3 = 0$ **3D:** $k_3 = 2$

Crossing waves

(a)   (b)

Parallel beating waves

(c)   (d)

Figure 13: Norm of the time-filtered wavenumber bispectrum. The filter is applied to the target sensor G_3, which spans all x locations. It retains either the frequencies associated with the low-frequency dynamics $(f_2 - f_1)$ (indicated in the legend with $G_3(f_2 - f_1)$) or those associated with the high-frequency dynamics $(f_2 + f_1)$ (indicated in the legend with $G_3(f_2 + f_1)$). Symbols are used when the lines overlap perfectly. The green diamond symbols indicate the presence of self-quadratic couplings, i.e. $f_1 + f_1 = 2f_1$ and $f_2 + f_2 = 2f_2$. The vertical black lines indicate the separation (solid) and reattachment (dashed) locations.

	$x_{forcing} < x < x_{sep}$	$x_{sep} < x < x_{reatt}$	$x > x_{reatt}$
Crossing waves 2D	0.98	0.53	0.76
Crossing waves 3D	0.57	0.52	0.52
Parallel beating waves 2D	-0.17	-0.17	0.12
Parallel beating waves 3D	0.52	0.52	0.53

Table 7: Value of the propagation velocity of the bispectral content normalised by the external velocity, i.e. U_B/U_∞, for each region of the flow: from the forcing location to the separation point, within the recirculating region and downstream the reattachment point.

2f_1 and 2f_2. In the time delay domain of Figure 14, the sum of these two waves of similar frequencies is visualised, through beating, as a wave at frequency $(f_1 + f_2)$ being modulated in amplitude by a wave at frequency $(f_1 - f_2)$. It hence results in spots of high frequency ripples with width equal to $T/2$ seen, for instance, in the first half of the separated region or

787 downstream of the reattachment point. In the Fourier space, however, the only contribution
788 to the $(f_2 - f_1)$ range comes from the quadratic interaction between modes 1 and 2.

789 Although barely visible, the same observations apply to the parallel beating waves in the
790 case of $k_3 = 2$ organisation of the flow (see panel (d)). Both crossing and parallel beating
791 waves cases for $k_3 = 0$ are free of this self quadratic interaction, since the self coupling of a
792 single mode towards zero wavenumber corresponds to zero frequency. Consequently, there
793 is no secondary modulation in time in panels (a) and (c).

794 In all these cases, the quadratic power couplings move from upstream to downstream, with
795 the exception of the 2D parallel beating waves. In this case, panel (c) clearly shows that there is
796 an upstream motion of period $T = 1/(f_2 - f_1)$ within the separated region. The corresponding
797 value of the propagation velocity is $U_B/U_\infty = -0.17$. Such a value is in agreement with the
798 values suggested by Larchevêque (2016), Bonne *et al.* (2019), and Threadgill *et al.* (2021).
799 Moreover it falls in the range of values observed in Mauriello *et al.* (2022), who studied
800 transitional SBLI in a similar flow configuration and observed an upstream motion from the
801 reattachment point towards the separation point. The value they found is $U_B/U_\infty = -0.09$ for
802 the features sustaining the low frequency dynamics and $U_B/U_\infty = -0.25$ for the frequencies
803 falling in the medium range. In our case, after $x = 197$, the direction of the motion changes
804 to downstream, with a speed of $U_B = 0.12 U_\infty$.

5.4. *Phenomenology of the non-linear interactions*

806 The basic phenomenology can now be proposed as follows. As the oblique modes convect
807 downstream in the separated shear layer, they grow in amplitude, developing a high amplitude
808 towards the end of the separation bubble, achieving a maximum quadratic power transfer.
809 After this power input, structures having zero spanwise wavenumber and period $T = 1/(f_2 -$
810 $f_1)$ split into two parts just upstream of the reattachment point. Part is convected downstream
811 with the reattaching flow, and is possibly reinforced by further quadratic interactions between
812 the oblique modes still persisting in that region. The other part enters the lower region of
813 separated zone and is subject to an upstream propagation up towards (and beyond) the
814 separation point. This upstream propagation occurs without further quadratic power supply
815 because of the low oblique mode amplitude in that region. The separation point and the
816 reattaching boundary layer therefore undergoes motion similar in amplitude but opposite in
817 sign. In this context, the work of Dupont *et al.* (2006) noted that the rear part of the interaction
818 for an oblique reflected shock geometry also exhibits some degree of unsteadiness which
819 is in quasi-linear dependence with the reflected shock motion, reinforcing the idea that the
820 separation bubble is in a breathing motion. In addition, the work of Touber & Sandham
821 (2009) on a turbulent shock-induced separation bubble interaction had already observed a
822 jump in the velocity phase associated with the wall pressure perturbations. However, in their
823 work, this jump is observed to occur at one-third of the length of the separation zone. In
824 the present work, the shift in the velocity direction occurs near the point of minimum C_f at
825 $x = 200$ (see Figure 7), after which the skin friction begins to increase. The same observation
826 applies to the other time delay maps, although instead of a net change in direction, an increase
827 in bispectral activity is observed.

828 We observed in Section 5.2 that, at the separation point, both crossing waves and parallel
829 beating waves experienced quadratic couplings towards wavenumber equal to zero (see
830 Figures 11 (a) and (c)). It is now possible to add that the nonlinearities observed at the
831 separation point in the case of parallel beating waves result from quadratic interactions of
832 the oblique modes which, after passing through the shock interaction, succeed in entering
833 the separation bubble via the reattachment point and traveling up to the separation point.
834 These triadic interactions result in 2D structures. In contrast, the 2D structures that populate
835 the separation point in the case of crossing waves are the result of quadratic interactions in

2D: $k_3 = 0$ **3D:** $k_3 = 2$
Crossing waves

(a)   (b)

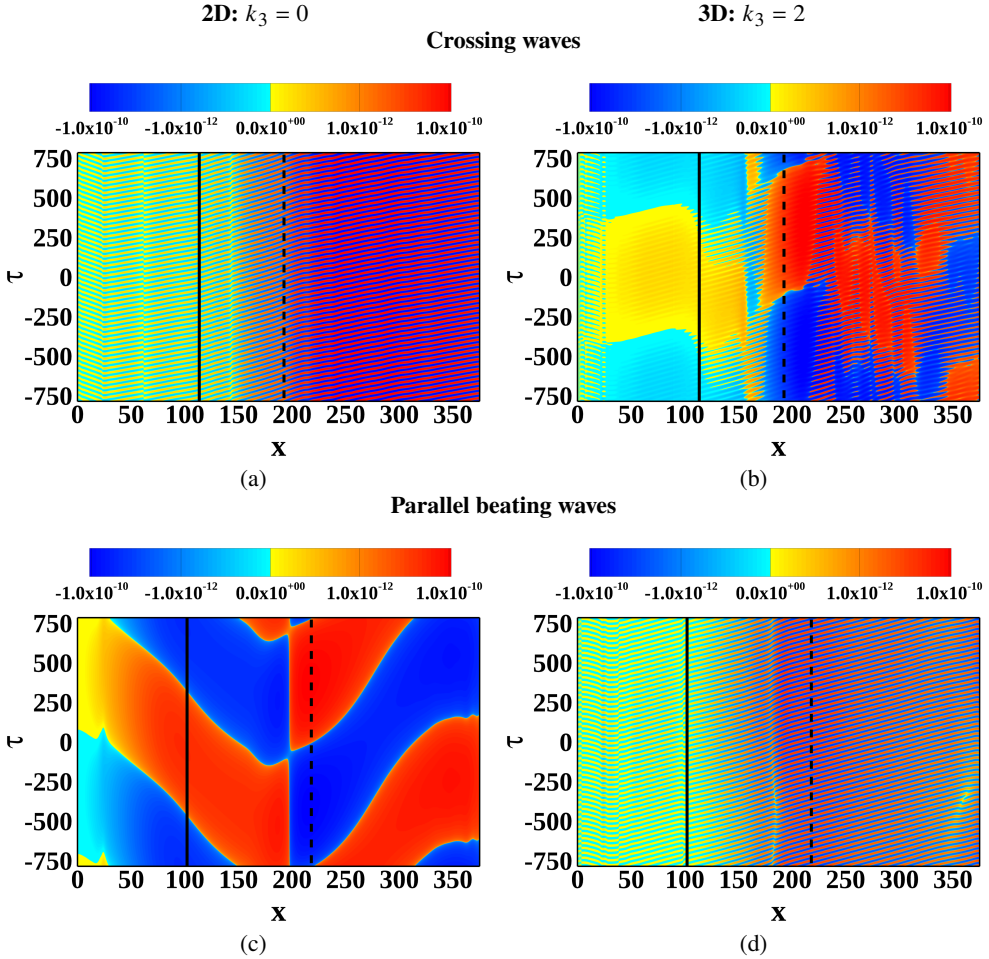**Parallel beating waves**

(c)   (d)

Figure 14: Time delay map extracted from the real part of the wavenumber bispectrum. First row shows the crossing waves, second row is for parallel beating waves. The vertical black lines indicate the separation (solid) and reattachment (dashed) points.

836 the incoming boundary layer. They begin to develop between the oblique modes and among
837 families of them.
838   Irrespective of the 2D or 3D spanwise structure of the flow and the specific arrangement
839 of the oblique modes in the two families, an upstream motion is observed for $x \leqslant 20$. This
840 point corresponds to the location of the forcing $x_{forcing}$, and since the perturbations are
841 introduced as density perturbations (leading to pressure perturbations), they are free to move
842 in all directions, including upstream within the subsonic layer of the compressible boundary
843 layer.

844   5.5. *The frequency-space organisation of the quadratic coupling*
845 The time delay τ introduced in equation 5.4 can be exploited to expand the wavenumber
846 bispectrum $Bis_{1,2,3}(k_{z_1}, k_{z_2}, \tau)$ into a Fourier series in time . This results in the frequency-
847 transformed wavenumber bispectrum $\widehat{Bis}_{1,2,3}(k_{z_1}, k_{z_2}, f_n)$ for discrete frequencies $f_n = n/T$
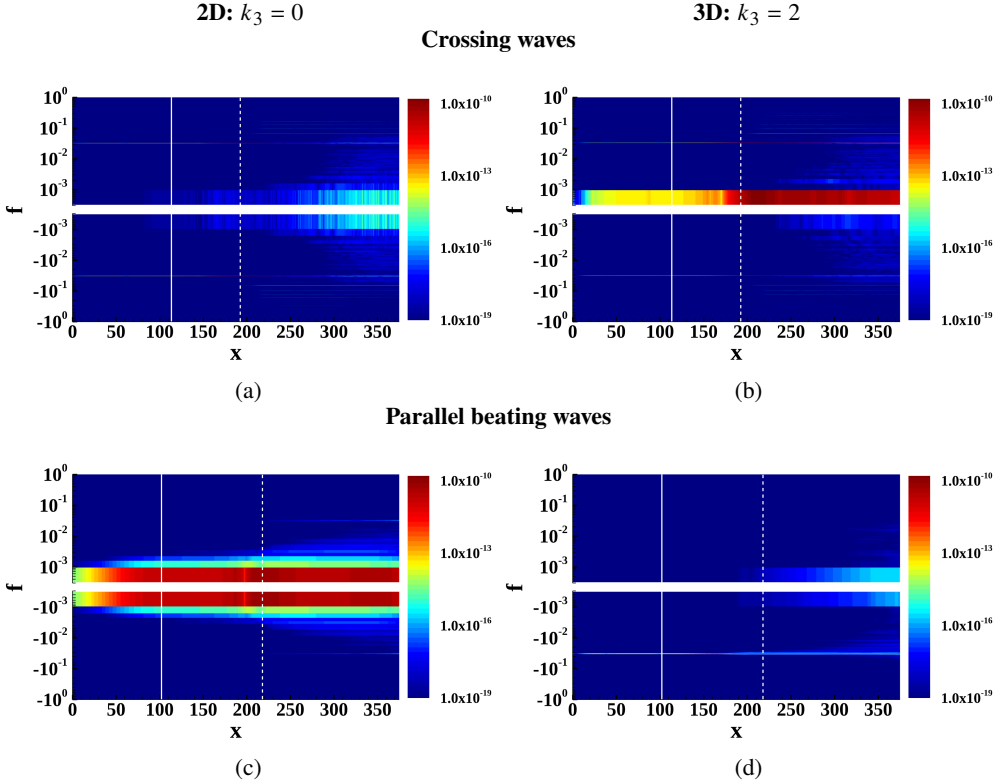848 such that

2D: $k_3 = 0$ **3D:** $k_3 = 2$

Crossing waves

(a)   (b)

Parallel beating waves

(c)   (d)

Figure 15: Streamwise-frequency distribution of norm of the frequency-transformed wavenumber bispectrum for selected wavenumver pairs.Panels (a)-(b): crossing waves; panels (c)-(d): parallel beating waves. The white vertical lines indicate the separation (solid) and reattachment (dashed) points.

$$Bis_{1,2,3}(k_{z_1}, k_{z_2}, \tau) = \sum_{n=-\frac{T}{2\Delta\tau}}^{+\frac{T}{2\Delta\tau}} \widehat{Bis}_{1,2,3}(k_{z_1}, k_{z_2}, f_n)\, e^{2i\pi\frac{n\tau}{T}} \tag{5.5}$$

850   The space transform provides information about the nature of the structures, while the
851 time transform allows the amount of non-linear content associated with each frequency and
852 each streamwise location to be determined. Overall, the frequency-transformed wavenumber
853 bispectrum directly highlights the relevant frequency content of the non-linear coupling
854 involved between selected wavenumbers. For simplicity, the subscript $_z$ is dropped in the
855 following discussion.

856   Figure 15 shows the norm of the space-frequency transformed bispectrum for each
857 combination of oblique waves. The streamwise organisation of the quadratic interactions
858 is plotted for each frequency. Only results for selected wavenumbers $k_1 + k_2 = k_3 = 0$
859 (left column) and $k_1 + k_2 = k_3 = 2$ (right column) are presented. Note that for $k_3 = 0$ the
860 wavenumber bispectrum is real, resulting in a time Fourier series that is even, i.e. symmetric
861 with respect to the origin $f = 0$. On the other hand, for $k_3 = 2$ the bispectrum is inherently
862 complex and the positive and negative frequency regions are no longer symmetric, even
863 in the Hermitian sense. If we take into account the asymmetries inherent in the different

arrangements of the waves, the present bispectra are therefore able to reflect these spanwise asymmetries.

In the case of the crossing wave family, panel (a) shows that from the reattachment point onwards, the quadratic coupling, associated with the transition mechanism, takes place. The cascade process starts from the forcing frequencies and fills the spectrum with exact non-linear harmonics of the fundamental frequency, becoming increasingly difficult to visualise in the plot because of their sharp frequency distribution and the use of the logarithmic scale. Evidence of quadratic interactions is clearly detected in the low-frequency range for $k_3 = 2$ (see panel (b)), and confirm the results presented in Table 6. Specifically, this confirms that two-dimensional flow features $k_3 = 0$ lack the low-frequency dynamics.

Panel (c) of figure 15 shows that high values of bispectral content are observed for parallel beating waves when $k_3 = 0$. Nevertheless, at the separation point as well as upstream and downstream of it, the range of frequency associated with quadratic couplings spreads up to $f \sim 0.005$. On the contrary, this combination of waves, when quadratically interacting to give $k_3 = 2$, does not support the low-frequency dynamics, and only the frequency corresponding to the sum of the forcing contribution emerges (see panel (d)). Note that this frequency is negative because the wavenumber $k_3 = 2$ under consideration is positive. For the parallel family, $k_3 = 2$ can be obtained from oblique modes only by considering an additive quadratic coupling, i.e. the one involving $k_1 = +\beta$ and $k_2 = +\beta$. It translates, through the *ansatz* (2.4)), into an $(-\omega_1, -\omega_2)$ coupling into the frequency space. As a consequence of the Hermitian symmetry of the space-time transform, the quadratic interaction resulting in the positive $(\omega_1 + \omega_2)$ frequency is found for the negative wavenumber $k_3 = -2$.

6. Additional considerations

So far we have focused on two cases with a difference-mode nonlinear interaction, in addition to the baseline case where the difference-mode was absent. In this section we expand the discussion to include two additional forcing configurations as well as a case with a different frequency combination.

6.1. *A beating crossing combination*

The spectral analysis of the pressure fluctuations at the wall showed that an approximately steady interaction (lacking 2D low frequency content) is observed in the case of the crossing waves family, while an unsteady interaction was found for the parallel beating arrangement. A third combination of waves that combines both parallel waves and crossing waves is next considered. The aim is to explore whether this new arrangement of waves still retains the properties of parallel waves to stimulate unsteadiness as well as the ability of crossing waves to facilitate the breakdown to turbulence. The arrangement is called *beating crossing* waves and it is expressed through the notation of (4.2) as

Beating crossing waves: $\rho'(x, z, t) = \rho_1'^+(x, z, t) + \rho_1'^-(x, z, t) + \rho_2'^+(x, z, t) + \rho_2'^-(x, z, t)$

Figure 16 (a) plots the streamwise evolution of the skin friction coefficient, comparing the different cases. The beating crossing waves have the shortest separation zone with $L_{int}/\delta^*_{inlet} = 44$ ($L_{sep}/\delta^*_{inlet} = 73.4$) and result in a transitioning boundary layer down-stream of the interaction. This result is consistent with the observation that this family possesses a double crossing wave combination and, as observed from the previous results, the breakdown to turbulence is facilitated.

Since double parallel beating waves are also included, low-frequency unsteadiness is
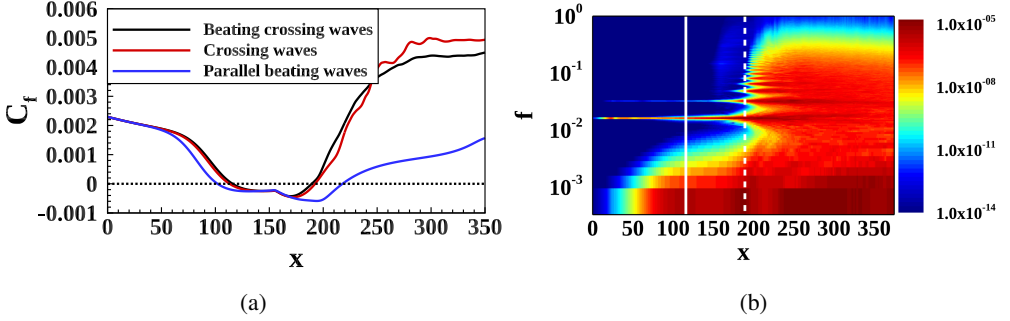
Figure 16: Figure (a) shows the streamwise evolution of the skin friction coefficient C_f for all combinations of waves. The black dashed horizontal lines indicates $C_f = 0$. Figure (b) plots the spectral decomposition of the wall pressure fluctuation for the sole beating crossing waves case. The white vertical lines indicate the separation (solid) and the reattachment (dashed) points.

expected to develop. Figure 16 (b) shows the spectral decomposition of the wall pressure fluctuations for the beating crossing waves. The same normalisation and structure of the spectra shown in Figure 8 is followed here. Downstream of the reattachment point and starting from the forcing frequencies, the energy content cascades over all their harmonics and fills the spectrum up to high frequencies consistent with the results extracted from the C_f plot that indicates transition to turbulence. When looking at the separation point, beating crossing waves shows high energy activity that results in an unsteady interaction. As observed, the parallel combination induces slow motion at $St_{L_{int}} = 0.037$. For the beating crossing family, the head shock moves at $St_{L_{int}} = 0.028$. This difference is due to the change of L_{int}. Hence, the inclusion of the parallel combination of the two wave families proves once again to be responsible for the slow 2D motion of the head shock, but this time combined with transition to turbulence. Note that all the quadratic metrics used in Section 5 to analyse the crossing and parallel cases have been applied to the beating crossing combination. The results, not presented here for the sake of conciseness, confirm that this more complex family combines the individual quadratic features of the two simpler cases.

6.2. *A streaky crossing combination*

Low speed velocity streaks are often present in laminar boundary layers, for example when free stream turbulence or roughness modifies the laminar base flow. They are steady in time ($\omega = 0$), but have non-zero spanwise wavenumber (Schmid & Henningson 2001). Hence it is of interest to take advantage of them to modify the simple crossing case to achieve a two-dimensional spanwise organisation of the flow at the separation point without altering the incoming frequency content and verify whether the slow bubble breathing motion occurs. The targeted non-linear coupling involving the streaks and the oblique modes will inherently result in the same frequency as the corresponding non-linear coupling between the sole oblique modes, but it must result in $k_z = 0$ in the separated flow region. Consequently, the spanwise dimension of the streaks must be carefully chosen. For this purpose, half of the spanwise dimension of the 3D unstable waves was chosen ($\beta_{streak} = 2\beta_{OM}$). The mathematical representation of the streaks is therefore given by $\rho'_{streak}(x, z, 0) = Re[A_0 \, \hat{\rho}(y)e^{i(2\beta z)}]$. By adding the streak to the crossing waves family, the new combination we are considering is called *streaky crossing* waves, and it is mathematically described by
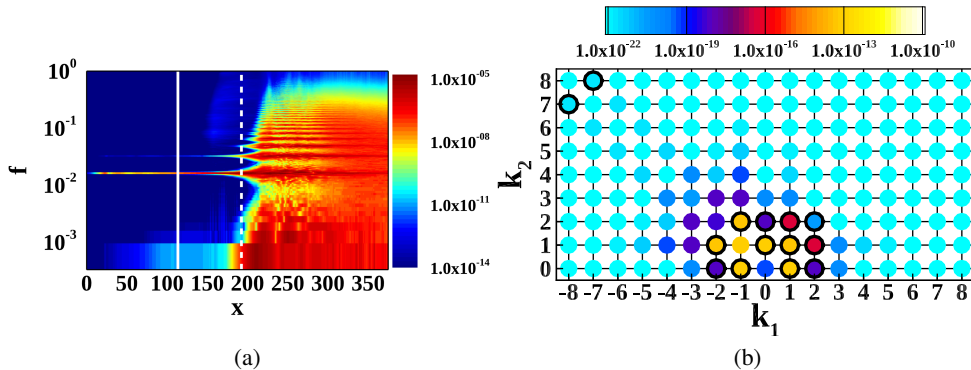
Figure 17: Streaky wave family: power spectra of the wall pressure fluctuations (panel (a)) and wavenumber bispectrum for sensor G_3 located at the separation point, denoted by the white solid vertical lines on plot (a).

Streaky crossing waves: $\rho'(x, z, t) = \rho_1'^+(x, z, t) + \rho_2'^-(x, z, t) + \rho_{streak}'(x, z, 0)$

By following the same mathematical approach presented in Section 5, for the streaky crossing family, we obtain that the only non-linear combination involving the oblique modes with frequency $(f_2 - f_1)$ is given by the same relation of (5.2). Nevertheless, if the contribution of the streak is included, many possible non-linear combinations of the triad of modes can result in the $(f_2 - f_1)$ frequency. The simplest ones are two consecutive quadratic coupling or a single cubic coupling. The five simplest possible non-linear couplings towards the low frequency range therefore read

$$f_{LF} = f_2 - f_1 \longleftrightarrow \begin{cases} \beta + \beta & = & 2\beta & \text{quadratic coupling} \\ (\beta + \beta) + 2\beta & = & 4\beta & \text{consecutive quadratic couplings} \\ (\beta + \beta) - 2\beta & = & 0 & \text{consecutive quadratic couplings} \\ \beta + \beta + 2\beta & = & 4\beta & \text{cubic coupling} \\ \beta + \beta - 2\beta & = & 0 & \text{cubic coupling} \end{cases} \qquad (6.1)$$

The first line corresponds to interactions between oblique modes only, whereas the four subsequent lines are related to couplings involving both the oblique modes and streaks. Thus, the streaky family potentially results at low frequency in both 2D and 3D flow features, once either quadratic or cubic couplings involving streaks are taken into account.

Figure 17 (a) shows the spectral content of the pressure fluctuations field extracted at the wall for the streaky crossing case. In contrast with the simple crossing arrangement, a low-frequency activity of mostly constant level is found in the separated flow region. It results in a low-frequency power at the separation point being 1.5 orders of magnitude larger for the streaky case compared to the original crossing case. Although such a value is more than four orders of magnitude lower than the one found for the parallel arrangement, it is a clear indication that streaks non-linearly promote flow structures at low frequency that are sustained in the separated flow region.

Recalling the results from Mauriello (2024) and from Section 5, it is tempting to postulate

	Low frequency		High frequency	
	$(\omega_2 - \omega_1)$	k_{LF}	$(\omega_2 + \omega_1)$	k_{HF}
Crossing waves:				
$(-\omega_1, \beta) \times (-\omega_2, -\beta)$	$\beta + \beta = 2\beta$	2	$\beta - \beta = 0$	0
Parallel beating waves:				
$(-\omega_1, \beta) \times (-\omega_2, \beta)$	$\beta - \beta = 0$	0	$-\beta - \beta = -2\beta$	−2
Beating crossing waves:				
$(-\omega_1, \pm\beta) \times (-\omega_2, \pm\beta)$	$\beta - \beta = 0$	0	$\beta + \beta = 2\beta$	2
	$\beta + \beta = 2\beta$	2	$\beta - \beta = 0$	0
	$-\beta - \beta = -2\beta$	−2	$-\beta + \beta = 0$	0
	$-\beta + \beta = 0$	0	$-\beta - \beta = -2\beta$	−2
Streaky crossing waves:				
$(-\omega_1, \beta) \times (-\omega_2, -\beta) \times (0, 2\beta)$	$\beta + \beta = 2\beta$	2	$\beta - \beta = 0$	0
	$\beta + \beta + 2\beta = 4\beta$	4	$\beta - \beta + 2\beta = 2\beta$	2
	$\beta + \beta - 2\beta = 0$	0	$\beta - \beta - 2\beta = -2\beta$	−2

Table 8: Summary of the couplings for all modal forcing combinations. The subscript "$_{LF}$" and "$_{HF}$" in k indicate the low frequency dynamics $(\omega_2 - \omega_1)$ and the high frequency dynamics $(\omega_2 + \omega_1)$ respectively.

that such a sustainability is related to two-dimensionality. Candidate non-linear couplings having such a property correspond to lines 3 and 5 of equation 6.1. The former, being quadratic in nature, can be tested using the bicoherence defined in equation 5.4. Its imprint on the $k_1 - k_2$ bispectral map at separation plotted in Figure 17 (b) would include the primary interaction between oblique modes at $(k_1, k_2) = (1, 1)$, already present in the simple crossing case, as well as the secondary interaction between the structures resulting from the primary interaction and the streaks at $(2, -2)$.

No such extra quadratic coupling is found when comparing Figures 11(a) and 17(b) and, in fact, the norms of the bispectra at separation are similar for the pure crossing and streaky crossing cases for all wavenumber pairs under consideration. This demonstrates that, at least in the separated region of the flow, streaks do not contribute to quadratic coupling. Moreover, bicoherence levels are generally lower for the streaky crossing case. This, coupled with similar norms for the bispectra, is a clear indication that the extra power found in the separated region for the streaky case in Figure 17 (a) do not originate from any additional quadratic coupling.

The cubic coupling hypothesis appears therefore as the most probable explanation. Note that it could be formally tested by computing the wavenumber trispectrum. However its definition involves four distinct time series, three time delays and only limited obvious hypotheses to reduce the dimension of the input space they span. This makes its computation quite cumbersome, even if restricted to a small number of wavenumber triads. As a consequence, a formal demonstration of the actual occurrence of cubic couplings involving streaks at the separation point has not been carried out.

Table 8 integrates table 6 with all possible combinations at both low frequency $(\omega_2 - \omega_1)$ and high frequency $(\omega_2 + \omega_1)$ for the new families of oblique mode, i.e. the beating crossing
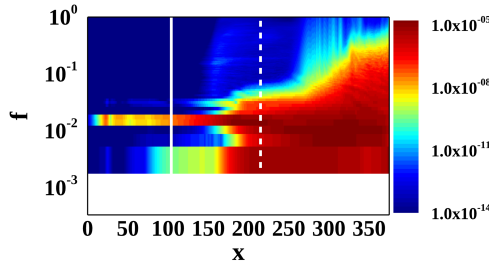
Figure 18: Power spectrum of the wall pressure fluctuations for the parallel beating waves family with forcing frequency difference $\Delta S_{L_{int}} \simeq 0.4$. The white vertical lines indicated the separation (solid) and the reattachment (dashed) points.

waves and streaky crossing waves. The table supports the results presented in Sections 6.1 and 6.2. When the arrangement of oblique modes, whether it contains a parallel arrangement and/or structures such that the resulting spanwise wavenumber (which interacts with the oblique modes) is $k_z = 0$ (as we have seen with the streak), then activity of low-frequecy spectral content appears in the spectrum at the separation point. Those 2D structures are responsible for the phenomenon of the low-frequency unsteadiness.

6.3. *Effect of the frequency*

At this point it is important to make a few more comments. First, both parallel beating waves and simple crossing wave configurations had the same injected energy level (see Table 3). Despite that, they exhibited very differing characteristics in terms of their influence on the unsteady dynamics and transition process. Secondly, regardless of the specific configuration, the system was forced with two high frequencies, such that their difference fell in the low range of the frequency spectrum, i.e. $\Delta St_{L_{int}} \simeq 0.04$. Although the forcing is set in the high frequency range, thanks to quadratic coupling we observed low-frequencies emerging in the spectrum. Nevertheless, it would be interesting to observe the possible consequences for both the low-frequency dynamics and the transition process when the resulting, quadratically-induced, Strouhal number falls within a higher range of the frequency spectrum. To this end, we decided to investigate the arrangement of parallel beating waves since they resulted in a strong response at the quadratic couplings in the low-frequency dynamics. The forcing frequency was chosen so that the frequency separating the motion of the two parallel wave families is ten times larger than for the original one, with $\Delta St_{L_{int}} \simeq 0.4$. This (similar) value was observed in the work of Mauriello (2024), which studied the interaction between an incoming laminar boundary layer and an impinging reflected shock system at $M = 1.7$, and examined the non-linear coupling between the multiple boundary layer modes and the flow features at the separation point. In that work, it was found that the resulting nonlinearities occurring between oblique modes of different frequencies were progressively damped when the frequency difference exceeded $\Delta St_{L_{int}} = 0.35$.

Figure 18 shows the power spectrum of the wall pressure fluctuations for the parallel beating waves with medium forcing frequency-difference yielding to $\Delta St_{L_{int}} \simeq 0.4$. For simplicity, in the following discussion we will refer to this case as MF-forcing, whereas the original parallel beating case with the low forcing frequency-difference of $\Delta St_{L_{int}} \simeq 0.04$, whose corresponding power spectrum is plotted in Figure 8 (b), will be referred to as LF-forcing.

When comparing Figures 8 (b) and 18, it appears that the region downstream the reattachment point experiences a different transition state, with a slightly more developed energy cascade in the case of MF-forcing. Such a difference is consistent with the slightly
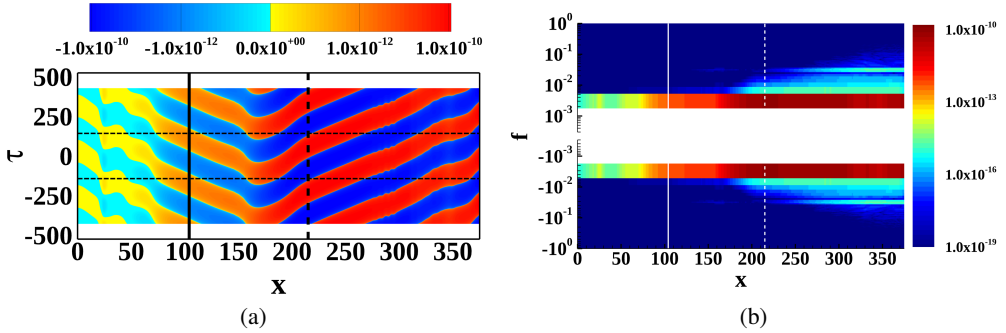
Figure 19: Wavenumber bispectra of the parallel beating waves family with forcing frequency difference $\Delta S_{L_{int}} \simeq 0.4$ for the 2D ($k_{z_3} = 0$) coupling: streamwise coordinate – time delay map if the real part (panel (a)) and norm of the time–Fourier transform (panel (b)). The vertical lines indicated the separation (solid) and the reattachment (dashed) points. The horizontal dashed lines in panel (a) denote the time boundary of a single period since data have been duplicated through time–periodicity for better visualization.

reduced size of the separated region in that case. One can postulate that the alteration of the early transition is due to the non-linear process that broadens the frequency ranges ω^n associated with the nth non-linear harmonics of the oblique modes. The broadening is progressively achieved through a succession of forward and backward interactions involving the two kinds of oblique modes: $(\omega^n) \times (\pm\omega_1) \rightarrow (\omega^n \pm \omega_1)$ followed by $(\omega^n \pm \omega_1) \times (\mp\omega_2) \rightarrow (\omega^n \pm \omega_1 \mp \omega_2)$. The frequency extent of the process therefore scales with the $(\omega_2 - \omega_1)$ difference, making the MF-forcing case to result more rapidly in the overlapping of the broadened frequency ranges, thus leading to a fuller spectrum at earlier stations.

Besides the transition mechanism, the larger frequency difference also affects the low-frequency dynamics. Note that the lack of energy content for frequencies below $f = 0.0035$ for the MF-forcing case is a direct consequence of the medium frequency-difference forcing that results in a periodicity in time being inversely proportional to $\Delta St_{L_{int}}$. The power contents of the lowest frequency ranges, being equal to $\Delta\omega/(2\pi)$ for both cases, is rather similar alongside the last third of the separated region ($180 < x < 220$) and downstream of the reattachment. In the first two thirds of the bubble, however, a significantly lower power is found for the MF-forcing case compared to the LF-forcing one.

The power content of the low frequency range in the separated region having been associated in Section 5, for the parallel case, with $2D$ quadratic coupling, the various bispectral metrics described in that section have also been applied to the MF-forcing case. Overall, these analyses yielded similar results to the ones of the LF-forcing case, but two noticeable differences were found in the separated region. The first is related to the upstream propagation velocity of the 2D bispectral content, which is found to be about 2.5 times larger than for the LF-forcing case, as deduced from the time delay map of the norm of the bispectrum for the $k_{z_3} = 0$ coupling, plotted in Figure 19 (a). It is worth noting that a similar velocity ratio was found in Mauriello *et al.* (2022) between the lower and upper frequency ranges of the low-frequency, upstream propagating structures resulting from quadratic interactions between multiples oblique modes.

Beyond a velocity change, the quadratically-induced structures of the MF-forcing case are also subject to an extra damping when moving upstream in the separated region. The norm of the time Fourier-transformed wavenumber bispectrum associated with the 2D ($k_3 = 0$) coupling experiences a 1.5 order of magnitude drop between $x = 180$ and $x = 155$, as seen in

Figure 19 (b). In the first half of the bubble this yields a difference of more than one order of magnitude between the bispectral powers at the lowest frequency found in the LF-forcing and MF-forcing cases. This fully explains the similar differences seen on the power spectrum in Figures 8 (b) and 18. It therefore seems that the downstream part of the separated region acts as a low-pass filter (in the wavenumber space) with respect to the 2D structures originating in the quadratic coupling of oblique modes. This is reminiscent of the the low-pass filter nature of the shock/bubble system suggested by Touber & Sandham (2011) for a turbulent interaction, even if the upstream part of the separated region was considered in this work. Moreover, this is compatible with the mechanism suggested by Bugeat *et al.* (2022).

7. Conclusions

The present work has provided a comprehensive investigation into the unsteady dynamics of transitional shock wave-boundary layer interactions (SBLIs) at Mach 1.5, employing direct numerical simulations, deterministic forcing and high-order spectral analysis. The study has successfully elucidated the distinct roles of different oblique mode configurations in triggering low-frequency unsteadiness and transition to turbulence. The results unequivocally demonstrate that these two phenomena are decoupled, with the transition to turbulence primarily driven by nonlinear interactions of high-frequency unstable modes (oblique breakdown), while low-frequency unsteadiness arises from the quadratic coupling of low-frequency components. The study further underscores the critical role of the specific arrangement of oblique modes in influencing the flow dynamics. The presence of crossing oblique modes, characterised by opposite orientation of spanwise wavenumbers, was found to facilitate the transition to turbulence. In contrast, parallel oblique modes, with the same orientation of spanwise wavenumber, were more effective in triggering low-frequency unsteadiness. The research also confirmed that the trace of low-frequency unsteadiness in wavenumber space is distinctly two-dimensional, originating from nonlinear interactions of oblique modes downstream of the shock interaction that subsequently propagate upstream within the separated flow region.

Additional mode configurations were explored. The beating crossing waves configuration, which combines aspects of both parallel and crossing waves, was shown to exhibit both low-frequency unsteadiness and transition to turbulence, confirming that these phenomena can coexist under certain conditions. Then the streaky crossing waves configuration was investigated, where low-speed streaks are added to the crossing waves. This configuration leads to low-frequency unsteadiness involving cubic interactions, further highlighting the role of 2D flow structures in this phenomenon.

Finally, the impact of forcing frequency was examined by considering a case where the difference between the forcing frequencies is increased. It is observed that, when the difference between the forcing frequencies falls within a specific range, identified as $\Delta St_{L_{int}} <$ 0.4, it facilitates the generation of low-frequency unsteadiness, suggesting that the bubble acts as a low-pass filter for nonlinear interactions.

The insights gleaned from this study contribute significantly to our understanding of the intricate dynamics of transitional SBLIs. The findings not only enhance our comprehension of the underlying mechanisms but also offer potential avenues for future research and the development of control strategies. For instance, the identification of specific oblique mode arrangements that favour or suppress low-frequency unsteadiness and turbulence transition could pave the way for flow control techniques aimed at mitigating the detrimental effects of SBLIs in high-speed flows. The observed two-dimensional nature of low-frequency unsteadiness in wavenumber space could also be leveraged to develop simplified models for predicting and controlling such fluctuations.

Author ORCIDs.
M. Mauriello, https://orcid.org/0000-0003-2064-0681
P. K. Sharma, https://orcid.org/0000-0003-2078-2559
L. Larchevêque, https://orcid.org/0000-0002-8588-1374
N. D. Sandham, https://orcid.org/0000-0002-5107-0944

REFERENCES

AGOSTINI, L., LARCHEVÊQUE, L., DUPONT, P., DEBIÈVE, J. F. & DUSSAUGE, J. P. 2012 Zones of influence and shock motion in a shock/boundary-layer interaction. *AIAA Journal* **50**, 1377–1387.

BABINSKY, H. & HARVEY, J. K. 2011 *Shock wave-boundary-layer interactions*, , vol. 32. Cambridge University Press.

BONNE, N.and BRION, V., GARNIER, E., BUR, R., MOLTON, P., SIPP, D. & JACQUIN, L. 2019 Analysis of the two-dimensional dynamics of a Mach 1.6 shock wave/transitional boundary layer interaction using a rans based resolvent approach. *Journal of Fluid Mechanics* **862**, 1166–1202.

BUGEAT, BENJAMIN, ROBINET, J-CH, CHASSAING, J-C & SAGAUT, PIERRE 2022 Low-frequency resolvent analysis of the laminar oblique shock wave/boundary layer interaction. *Journal of Fluid Mechanics* **942**, A43.

CHANDOLA, G., HUANG X. & ESTRUCH-SAMPER, D. 2017 Highly separated axisymmetric step shock-wave/turbulent-boundary-layer interaction. *Journal of Fluid Mechanics* **828**, 236–70.

CLEMENS, NOEL T & NARAYANASWAMY, VENKATESWARAN 2014 Low-frequency unsteadiness of shock wave/turbulent boundary layer interactions. *Annual Review of Fluid Mechanics* **46**, 469–492.

DÉLERY, JEAN, MARVIN, JOHN G & RESHOTKO, ELI 1986 Shock-wave boundary layer interactions. AGARD.

DOERFFER, PIOTR, HIRSCH, CHARLES, DUSSAUGE, JEAN-PAUL, BABINSKY, HOLGER & BARAKOS, GEORGE N 2010 *Unsteady effects of shock wave induced separation*, , vol. 114. Springer Science & Business Media.

DOLLING, DS & MURPHY, MT 1983 Unsteadiness of the separation shock wave structure in a supersonic compression ramp flowfield. *AIAA Journal* **21** (12), 1628–1634.

DOLLING, DAVID S 2001 Fifty years of shock-wave/boundary-layer interaction research: what next? *AIAA journal* **39** (8), 1517–1531.

DUPONT, P., HADDAD, C. & DEBIÈVE, J. F. 2006 Space and time organization in a shock-induced separated boundary layer. *Journal of Fluid Mechanics* **559**, 255–277.

DUSSAUGE, JEAN-PAUL, DUPONT, PIERRE & DEBIÈVE, JEAN-FRANCOIS 2006 Unsteadiness in shock wave boundary layer interactions with separation. *Aerospace Science and Technology* **10** (2), 85–91.

ERENGIL, MEHMET ERDAL 1993 *Physical causes of separation shock unsteadiness in shock wave/turbulent boundary layer interactions*. The University of Texas at Austin.

ERENGIL, MEHMET E & DOLLING, DAVID S 1991 Unsteady wave structure near separation in a mach 5 compression rampinteraction. *AIAA journal* **29** (5), 728–735.

GANAPATHISUBRAMANI, BHARATHRAM, CLEMENS, NT & DOLLING, DS 2007 Effects of upstream boundary layer on the unsteadiness of shock-induced separation. *Journal of Fluid Mechanics* **585**, 369–394.

GANAPATHISUBRAMANI, B, CLEMENS, NT & DOLLING, DS 2009 Low-frequency dynamics of shock-induced separation in a compression ramp interaction. *Journal of Fluid Mechanics* **636**, 397–425.

GUIHO, FLORIAN, ALIZARD, FRÉDÉRIC & ROBINET, J-CH 2016 Instabilities in oblique shock wave/laminar boundary-layer interactions. *Journal of Fluid Mechanics* **789**, 1–35.

JENQUIN, C., JOHNSON E. C. & NARAYANASWAMY, V. 2023 Investigations of shock–boundary layer interaction dynamics using high-bandwidth pressure field imaging. *Journal of Fluid Mechanics* **961**, A5.

LARCHEVÊQUE, LIONEL 2016 Low-and medium-frequency unsteadinesses in a transitional shock–boundary reflection with separation. In *54th AIAA aerospace sciences meeting*, p. 1833.

36

LEE, BHK 2001 Self-sustained shock oscillations on airfoils at transonic speeds. *Progress in Aerospace Sciences* **37** (2), 147–196.

LUSHER, DAVID J, JAMMY, SATYA P & SANDHAM, NEIL D 2021 Opensbli: Automated code-generation for heterogeneous computing architectures applied to compressible fluid dynamics on structured grids. *Computer Physics Communications* **267**, 108063.

MAURIELLO, MARIADEBORA 2024 Non-linearities in the low-frequency dynamics of transitonal shock wave-boundary layer interactions. PhD thesis.

MAURIELLO, MARIADEBORA, LARCHEVÊQUE, LIONEL & DUPONT, PIERRE 2022 Non-linearities in transitional shock wave/boundary layer interactions. In *12th International Symposium on Turbulence and Shear Flow Phenomena*. Osaka (Japan), Japan.

MAYER, CHRISTIAN SJ, WERNZ, STEFAN & FASEL, HERMANN F 2011 Numerical investigation of the nonlinear transition regime in a mach 2 boundary layer. *Journal of fluid mechanics* **668**, 113–149.

NIESSEN, SÉBASTIEN EM, GROOT, KOEN J, HICKEL, STEFAN & TERRAPON, VINCENT E 2023 Convective instabilities in a laminar shock-wave/boundary-layer interaction. *Physics of Fluids* **35** (2).

PIPONNIAU, SÉBASTIEN, DUSSAUGE, JEAN-PAUL, DEBIEVE, JEAN-FRANÇOIS & DUPONT, PIERRE 2009 A simple model for low-frequency unsteadiness in shock-induced separation. *Journal of Fluid Mechanics* **629**, 87–108.

PIROZZOLI, SERGIO & GRASSO, FRANCESCO 2006 Direct numerical simulation of impinging shock wave/turbulent boundary layer interaction at m= 2.25. *Physics of fluids* **18** (6).

PRIEBE, STEPHAN & MARTÍN, M PINO 2012 Low-frequency unsteadiness in shock wave-turbulent boundary layer interaction. *Journal of Fluid Mechanics* **699**, 1–49.

PRIEBE, STEPHAN, TU, JONATHAN H, ROWLEY, CLARENCE W & MARTÍN, M PINO 2016 Low-frequency dynamics in a shock-induced separated flow. *Journal of Fluid Mechanics* **807**, 441–477.

PUCKETT, S. & NARAYANASWAMY, V. 2024 High-bandwidth pressure field imaging of fin-generated shock wave–boundary layer interactions. *Journal of Fluid Mechanics* **999**, A80.

ROBINET, J-CH 2007 Bifurcations in shock-wave/laminar-boundary-layer interaction: global instability approach. *Journal of Fluid Mechanics* **579**, 85–112.

SAÏDI, ISMAÏL BEN HASSAN, WANG, STÉPHANE, FOURNIER, GUILLAUME, TENAUD, CHRISTIAN & ROBINET, JEAN-CHRISTOPHE 2025 Modal analysis of the triadic interactions in the dynamics of a transitional shock wave boundary layer interaction. *Journal of Fluid Mechanics* **1009**, A43.

SANSICA, A. 2015 Stability and unsteadiness of transitional shock-wave/boundary-layer interactions in supersonic flows. PhD thesis, University of Southampton.

SANSICA, A, SANDHAM, ND & HU, Z 2014 Forced response of a laminar shock-induced separation bubble. *Physics of Fluids* **26** (9).

SANSICA, A., SANDHAM, N. D. & HU, Z. 2016 Instability and low-frequency unsteadiness in a shock-induced laminar separation bubble. *Journal of Fluid Mechanics* **798**, 5–26.

SCHMID, PJ & HENNINGSON, DS 2001 Stability and transition in shear flows. *New York* .

SMITS, ALEXANDER J & DUSSAUGE, JEAN-PAUL 2006 *Turbulent shear layers in supersonic flow*. Springer Science & Business Media.

SOUVEREIN, LJ, VAN OUDHEUSDEN, BW, SCARANO, F & DUPONT, P 2009 Application of a dual-plane particle image velocimetry (dual-piv) technique for the unsteadiness characterization of a shock wave turbulent boundary layer interaction. *Measurement Science and Technology* **20** (7), 074003.

THOMAS, FO, PUTNAM, CM & CHU, HC 1994 On the mechanism of unsteady shock oscillation in shock wave/turbulent boundary layer interactions. *Experiments in Fluids* **18** (1-2), 69–81.

THREADGILL, JAMES AS, LITTLE, JESSE C & WERNZ, STEFAN H 2021 Transitional shock boundary layer interactions on a compression ramp at mach 4. *AIAA journal* **59** (12), 4824–4841.

TOUBER, EMILE & SANDHAM, NEIL D 2009 Large-eddy simulation of low-frequency unsteadiness in a turbulent shock-induced separation bubble. *Theoretical and computational fluid dynamics* **23**, 79–107.

TOUBER, EMILE & SANDHAM, NEIL D 2011 Low-order stochastic modelling of low-frequency motions in reflected shock-wave/boundary-layer interactions. *Journal of Fluid Mechanics* **671**, 417–465.

TYNAN, G. R., MOYER, R. A., BURIN, M. J. & HOLLAND, C. 2001 On the nonlinear turbulent dynamics of shear-flow decorrelation and zonal flow generation. *Physics of Plasmas* **8**, 2691–2699.

UENALMIS, O & DOLLING, D 1994 Decay of wall pressure field and structure of a mach 5 adiabatic turbulent boundary layer. In *Fluid Dynamics Conference*, p. 2363.

WU, MINWEI & MARTIN, M PINO 2008 Analysis of shock motion in shockwave and turbulent boundary layer interaction using direct numerical simulation data. *Journal of Fluid Mechanics* **594**, 71–83.